A&A 663, A174 (2022)
https://doi.org/10.1051/0004-6361/202142469

Astronomy & Astrophysics

Disc dichotomy signature in the vertical distribution of [Mg/Fe] and the delayed gas infall scenario

E. Spitoni[1,2,3], V. Aguirre Børsen-Koch[3], K. Verma[4,3], and A. Stokholm[5,6,3]

[1] Université Côte d'Azur, Observatoire de la Côte d'Azur, CNRS, Laboratoire Lagrange, Bd de l'Observatoire, CS 34229, 06304 Nice Cedex 4, France
e-mail: emanuele.spitoni@oca.eu
[2] Konkoly Observatory, Research Centre for Astronomy and Earth Sciences, Eötvös Loránd Research Network (ELKH), Konkoly Thege M. út 15-17, 1121 Budapest, Hungary
[3] Stellar Astrophysics Centre, Department of Physics and Astronomy, Aarhus University, Ny Munkegade 120, 8000 Aarhus C, Denmark
[4] Instituto de Ciencias del Espacio (ICE, CSIC), Campus UAB, Carrer de Can Magrans, s/n, 08193 Cerdanyola del Valles, Spain
[5] Dipartimento di Fisica e Astronomia, Università degli Studi di Bologna, Via Gobetti 93/2, 40129 Bologna, Italy
[6] INAF – Osservatorio di Astrofisica e Scienza dello Spazio di Bologna, Via Gobetti 93/3, 40129 Bologna, Italy

Received 18 October 2021 / Accepted 13 April 2022

ABSTRACT

Context. Analysis of the Apache Point Observatory Galactic Evolution Experiment project (APOGEE) data suggests the existence of a clear distinction between two sequences of disc stars in the [α/Fe] versus [Fe/H] abundance ratio space, known as the high- and low-α sequence, respectively. This dichotomy also emerges from an analysis of the vertical distribution of the [α/Fe] abundance ratio.
Aims. We aim to test whether the revised two-infall chemical evolution models designed to reproduce the low- and high-α sequences in the [α/Fe] versus [Fe/H] ratios in the solar neighbourhood are also capable of predicting the disc bimodality observed in the vertical distribution of [Mg/Fe] in APOGEE DR16 data.
Methods. Along with the chemical composition of the simple stellar populations born at different Galactic times predicted by our reference chemical evolution models in the solar vicinity, we provide their maximum vertical height above the Galactic plane $|z_{\rm max}|$ computed assuming the relation between the vertical action and stellar age in APOGEE thin-disc stars.
Result. The vertical distribution of the [Mg/Fe] abundance ratio predicted by the reference chemical evolution models is in agreement with that observed when combining the APOGEE DR16 data (chemical abundances) with the astroNN catalogue (stellar ages, orbital parameters) for stars younger than 8 Gyr (only low-α sequence stars). Including the high-α disc component, the dichotomy in the vertical [Mg/Fe] abundance distribution is reproduced considering the observational cut in the Galactic height of $|z| < 2$ kpc. However, our model predicts an overly flat (almost constant) growth of the maximum vertical height $|z_{\rm max}|$ quantity as a function of [Mg/Fe] for high-α objects in contrast with the median values from APOGEE data. Possible explanations for such a tension are that: (i) the APOGEE sample with $|z| < 2$ kpc is more likely than ours to be contaminated by halo stars, causing the median values to be kinematically hotter, and (ii) external perturbations – such as minor mergers – that the Milky Way experienced in the past could have heated up the disc, and the heating of the orbits cannot be modeled by only scattering processes. Assuming a disc dissection based on chemistry for APOGEE-DR16 stars ($|z| < 2$ kpc), the observed $|z_{\rm max}|$ distributions for high-α and low-α sequences are in good agreement with our model predictions if we consider the errors in the vertical action estimates in the calculation. Moreover, a better agreement between predicted and observed stellar distributions at different Galactic vertical heights is achieved if asteroseismic ages are included as a constraint in the best-fit model calculations.
Conclusions. The signature of a delayed gas infall episode, which gives rise to a hiatus in the star formation history of the Galaxy, are imprinted both in the [Mg/Fe] versus [Fe/H] relation and in vertical distribution of [Mg/Fe] abundances in the solar vicinity.

Key words. Galaxy: abundances – Galaxy: evolution – Galaxy: disk – Galaxy: kinematics and dynamics – ISM: general

1. Introduction

Analysis of the Apache Point Observatory Galactic Evolution Experiment project (APOGEE) data (Nidever et al. 2014; Hayden et al. 2015; Ahumada et al. 2020; Queiroz et al. 2020; Vincenzo et al. 2021) highlighted the presence of two distinct sequences in the [α/Fe] versus [Fe/H] abundance ratio space for disc stars: the so-called high-α sequence, classically associated with an old population of stars in the thick disc, and the low-α sequence, which is mostly comprised of relatively young stars in the thin disc. This dissection has also been revealed by other observational campaigns: the *Gaia*-ESO survey (e.g., Recio-Blanco et al. 2014; Rojas-Arriagada et al. 2016, 2017) and the Archéologie avec Matisse Basée sur les aRchives de l'ESO project (AMBRE; Mikolaitis et al. 2017; Santos-Peral et al. 2021), the Galactic Archaeology with HERMES survey (GALAH; Buder et al. 2019, 2021), and the Large sky Area Multi Object fiber Spectroscopic Telescope (LAMOST; Yu et al. 2021).

Cosmological hydrodynamic simulations of Milky Way-like galaxies (Kobayashi & Nakasato 2011; Snaith et al. 2016) predict such a bimodality in the distribution of chemical elements. While in Vincenzo & Kobayashi (2020) this dichotomy is mainly attributed to the interplay between infall and ouflow

events, in the dynamical model presented by Clarke et al. (2019) it arises from fragmentation of the early gas-rich disc. On the other hand, in several theoretical models of Galactic disc evolution, it has been proposed that this bimodality is strictly connected to a delayed gas-accretion episode of primordial composition (i.e. Noguchi 2018; Buck 2020; Lian et al. 2020; Khoperskov et al. 2021; Agertz et al. 2021). Moreover, the AURIGA simulations presented by Grand et al. (2018) clearly point out that a bimodal distribution in the [Fe/H]–[α/Fe] plane is a consequence of a significantly lowered gas accretion rate at ages between 6 and 9 Gyr. Verma et al. (2021) compared AURIGA simulations with 7000 stars for which asteroseismic, spectroscopic, and astrometric data are available, and concluded that the emerged abundance dichotomies in the [α/Fe] versus [Fe/H] plane appear to be qualitatively similar to observations.

Spitoni et al. (2019b) and Spitoni et al. (2020, hereafter ES20) revised the classical two-infall chemical evolution model (Chiappini et al. 1997) in order to reproduce the APOKASC (APOGEE+ *Kepler* Asteroseismology Science Consortium, Silva Aguirre et al. 2018) sample. These authors invoked the presence of a delayed gas infall episode (~4 Gyr) in order to reproduce the high- and low-α sequence stars, including precise asteroseismic ages as a constraint. This delayed infall of gas gives rise to the low-α sequence by bringing pristine metal-poor gas into the system which dilutes the metallicity of interstellar medium while keeping [α/Fe] abundance almost unchanged. Similarly, Spitoni et al. (2021, herafter ES21) also found the significant delay between the two gas infall episodes to be fundamental in order to reproduce APOGEE DR16 data in the solar vicinity, whereas in the innermost regions a chemically enriched gas infall is required in order to reproduce observed [Mg/Fe] versus [Fe/H] ratios as also suggested by Palla et al. (2020).

An inside-out formation of the thin disc of the Galaxy naturally emerges from the multi-zone chemical evolution model of ES21, that is, the inner regions of the Milky Way formed on a much shorter timescale than the outer regions. Such a mechanism has also been found in complex cosmological simulations of galaxy formation (Brook et al. 2012; Bird et al. 2013; Kobayashi & Nakasato 2011; Vincenzo & Kobayashi 2020). As underlined by Bird et al. (2013), the growth of the simulated galaxy also follows an 'upside-down' evolution in the vertical direction, namely old stars form in a relatively thick component and are kinematically heated very quickly after their birth. Later on, low-α stellar populations form in successively thinner discs. In principle, this is in agreement with the assumptions of the two-infall model, with shorter timescales of gas accretion characterising the formation of the thick disc. However, the above-mentioned ES20 and ES21 models can only be used to make predictions on projected quantities on the Galactic plane. Our principal aim with the present work is to study the vertical distribution of chemical elements assuming simplified dynamical prescriptions using these chemical evolution models.

In fact, in order to better understand the processes that dominated the formation and evolution of the Galactic disc, it is crucial to also compare model predictions with the observed vertical [α/Fe] distribution of stars at different heights above the Galactic plane. Indeed, the vertical abundance gradients have been the subject of several previous investigations. For instance, Schlesinger et al. (2014) analysed G dwarfs from the Sloan Extension for Galactic Understanding and Exploration (SEGUE) survey, and revealed a negligible vertical metallicity gradient in the Milky Way disc for different [α/Fe] subsamples. This suggests that stars that formed in different epochs shared similar star formation processes and evolution. Mikolaitis et al. (2014) used the spectra of around 2000 FGK dwarfs and giants from the *Gaia*-ESO survey iDR1, and found that thick-disc stars show a shallower vertical metallicity gradient than those of the thin disc, an opposite [α/Fe] ratio gradient to that of the thin disc, and positive vertical individual [α/M] and [Al/M] gradients (where M is the metallicity). Duong et al. (2018) used data from the GALAH survey to determine the vertical properties of the Galactic thin and thick discs near the solar neighbourhood. The median [α/M] increases as a function of height, as noted previously by Schlesinger et al. (2014) and Mikolaitis et al. (2014). However, unlike the metallicity, they find that the α-abundance profile does not vary smoothly with $|z|$.

In addition to the chemical signatures, the orbital properties of stars, and in particular the change of dynamical actions over time, could provide important constraints on the main evolutionary processes that have determined stellar redistribution. Beane et al. (2018) and Ness et al. (2019) discuss the connections between dynamical actions, ages, and chemical abundances in disc stars. In particular, Gandhi & Ness (2019) found that, at all ages, the high- and low-α sequences are dynamically distinct and that selections in the action space can provide an efficient method to separate distinct dynamical populations.

More recently, Vincenzo et al. (2021) highlighted the presence of bimodality in the vertical [α/Fe] distribution of APOGEE DR16 that can be well modelled by adopting a double Gaussian stellar distribution: one component describing the low-α population with scale height $z_1 = 0.45$ kpc and one describing the high-α population with scale height $z_2 = 0.95$ kpc.

In the present article, we compare the vertical structure of the [Mg/Fe] distribution as emerging from APOGEE DR16 data in the solar neighbourhood with the results of revised two-infall chemical evolution models presented by ES20 and ES21. To do so, in addition to the predicted chemical composition of simple stellar populations (SSPs, defined as an assembly of coeval and chemically homogeneous stars) formed at different Galactic times, we provide the respective orbital parameters (i.e. maximum vertical height above the Galactic plane $|z_{\rm max}|$) computed using the recent relation between the vertical action J_z and stellar age found for APOGEE thin-disc stars (Ting & Rix 2019). The main aim of this work is to investigate whether or not the disc bimodality found in APOGEE DR16 stars in the [α/Fe] versus Galactic vertical height (Vincenzo et al. 2021) can also be interpreted as the signature of a delayed accretion of gas which happened about ~4.3 Gyr after formation of the Milky Way.

The paper is organised as follows. In Sect. 2, the observational data are presented. In Sect. 3, we outline the main characteristics of the reference chemical evolution models for the high- and low-α adopted in this study. In Sect. 4, we describe the adopted methodology to compute $|z_{\rm max}|$ for stars born at different Galactic times and the vertical [Mg/Fe] gradient. In Sect. 5, we present our results and finally, in Sect. 6, we draw our conclusions.

2. APOGEE DR16 data and the astroNN catalogue

In this study, we consider Mg and Fe abundances provided by APOGEE DR16 (Ahumada et al. 2020) for investigating the region with Galactocentric distances between 6 and 10 kpc as computed by Leung & Bovy (2019) and reported in the value-added astroNN[1] catalogue. We note that astroNN is deep-learning software that was applied to APOGEE DR16 spectra in

[1] https://data.sdss.org/sas/dr16/apogee/vac/apogee-astronn

order to determine stellar parameters, distances (Leung & Bovy 2019), and ages (Mackereth et al. 2019). In addition, the above-mentioned catalogue includes some of the most important orbital properties for stars (i.e. eccentricities, peri/apocenter radii, maximal disc height $|z_{\rm max}|$, orbital actions, frequencies, and angles) computed by Mackereth & Bovy (2018) assuming the `MWPotential2014` gravitational potential from Bovy (2015).

Following ES21, we choose only stars that are part of the Galactic disc with the same quality cuts suggested in Weinberg et al. (2019) assuming signal-to-noise ratio $(S/N) > 80$, and logarithm of surface gravity between $1.0 < \log g < 2.0$. In this study, we analyse different regions above and below the Galactic planes, considering stars with observed vertical heights of $|z| < 0.5$ kpc, $|z| < 1$ kpc, and $|z| < 2$ kpc in order to better analyse the vertical structure. In Fig. 1, we note that the vertical distribution with $|z| < 2$ kpc closely resembles the behaviour of the whole APOGEE-DR16 stellar sample in the region with Galactocentric distances enclosed between 6 and 10 kpc.

As underlined by Weinberg et al. (2019), the adopted selection in $\log g$ leaves only stars on the upper red giant branch (RGB), that is, the most luminous ones; it ensures that the stars in our sample can be observed by APOGEE over most of the distance range considered in this study, minimising distance-dependent changes in the population being analysed.

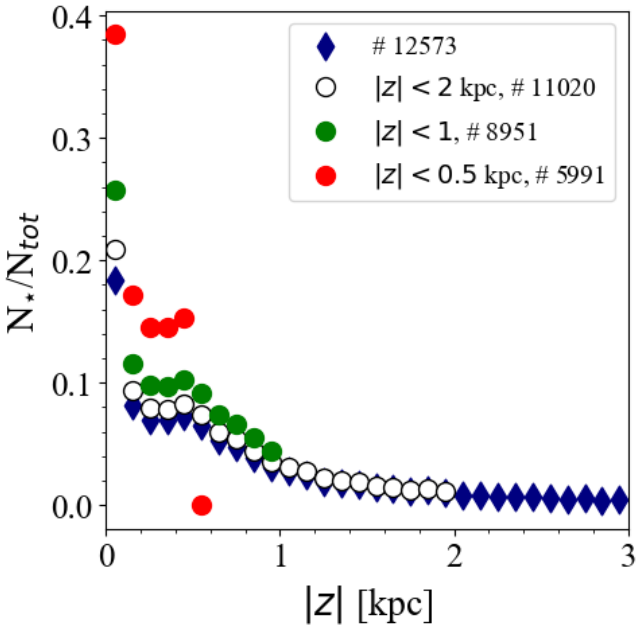

Fig. 1. Normalised distributions of the vertical height $|z|$ above the Galactic plane for APOGEE-DR16 adopting the selection cuts presented in Sect. 2. White, green, and red circles stand for distributions assuming $|z| < 2$ kpc, $|z| < 1$ kpc, and $|z| < 0.5$ kpc, respectively. The case without any cut in the vertical height is labelled with the blue diamonds. The respective total number of stars is also indicated.

3. Chemical evolution models for solar vicinity

In this section, we introduce the main assumptions of the two-infall chemical evolution model proposed by ES20 and ES21, providing a few details on the parametrisation of the infall and star formation. In both models, the Milky Way disc is assumed to be formed by two distinct episodes of gas accretion onto the Galactic plane (i.e. with null vertical height, $z = 0$ kpc). The gas infall rate is expressed as follows:

$$\mathcal{I}_i(t, z = 0) \equiv (X_i)_{\rm inf} \left[\mathcal{A}_1 \, e^{-t/t_1} + \theta(t - t_{\rm max}) \mathcal{A}_2 \, e^{-(t-t_{\rm max})/t_2} \right], \quad (1)$$

where t_1 and t_2 are the infall timescales for the thick and thin disc components, respectively. The coefficient $t_{\rm max}$ indicates the delay of the beginning of the second infall, hence the time for the maximum accretion rate on the second infall episode. Finally, the quantities $\mathcal{A}_1$ and $\mathcal{A}_2$ are obtained imposing a fit to the observed current total surface mass density in the solar neighbourhood. For the total surface density in the solar neighborhood, we adopted the value of $47.1 \pm 3.4 \, M_\odot \, {\rm pc}^{-2}$ suggested by McKee et al. (2015). We stress that these chemical evolution models do not make any assumption about the vertical growth of the gaseous and stellar discs.

In both ES20 and ES21 models, the numerical treatment is based on the Matteucci chemical evolution code (all the details could be retrieved in the review Matteucci 2021 and in the book Matteucci 2012). The star formation rate (SFR) is expressed as the Kennicutt (1998) law, $\psi \propto \nu \sigma_g^k$, where σ_g is the gas surface density, and $k = 1.5$ is the exponent. The quantity ν is the star formation efficiency (SFE), which is fixed to the values of $\nu_1 = 2 \, {\rm Gyr}^{-1}$ and $\nu_2 = 1 \, {\rm Gyr}^{-1}$ for the high-α and low-α sequences, respectively (see Table 1). The type Ia SN rate was computed following Greggio & Renzini (1983) and Matteucci & Greggio (1986) prescriptions (see Spitoni et al. 2009 for the rate expression).

Although the disc bimodality in the [α/Fe] versus [Fe/H] space in a simulated Milky Way-like galaxy in the cosmological framework of Vincenzo & Kobayashi (2020) is attributed to the interplay between infall and ouflow events, in ES20 and ES21 no Galactic winds were considered. This choice was motivated by the studies of Melioli et al. (2008, 2009) and Spitoni et al. (2008, 2009) on the Galactic fountains (i.e. processes originated by the explosions of Type II SNe in OB associations). These authors found that metals fall back close to the same Galactocentric region from which they are ejected and therefore do not significantly modify the chemical evolution of the disc as a whole.

The adopted nucleosynthesis prescriptions are the ones suggested by François et al. (2004). We briefly recall here the main assumptions for the chemical elements analysed in our study (i.e. Mg and Fe). The authors modified the Mg yields from massive stars from Woosley & Weaver (1995) to reproduce the solar abundance value. Mg yields from stars in the range 11–20 $M_\odot$ have been increased by a factor of seven whereas those from stars in the mass range $20 \, M_\odot < M < 100 \, M_\odot$ are lower than those predicted by Woosley & Weaver (1995) by a factor of two on average. No modifications are needed for the yields of Fe, as computed for solar chemical composition. The complete grid of the modified yields can be retrieved from Table 1 of François et al. (2004).

Concerning Type Ia SNe, the theoretical Mg yields by Iwamoto et al. (1999) have been increased by a factor of five in order to preserve the observed pattern of [Mg/Fe] versus [Fe/H]. The assumed IMF contains far fewer massive stars than other works in the community, and this affects the Mg enrichment, requiring more Mg from Type Ia SNe. The prescription for single low- and intermediate-mass stars is from van den Hoek & Groenewegen (1997) for the case of the mass-loss parameter which varies with metallicity (see Chiappini et al. 2003, model5).

The choice of such ad hoc nucleosynthesis prescriptions is supported by the fact that stellar yields are still a relatively uncertain component of chemical evolution models

(Romano et al. 2010). This set of yields has been used many times in the past by the Matteucci group in Trieste (see Matteucci 2021) and was found to be able to reproduce the main features of the solar neighbourhood (e.g., Cescutti et al. 2007; Spitoni & Matteucci 2011; Mott et al. 2013; Spitoni et al. 2014, 2017, 2015, 2019a,b; Vincenzo et al. 2019). Updated nucleosynthesis prescriptions for massive stars in the Galactic chemical evolution of Mg still show problems in reproducing the stellar data. For instance, Prantzos et al. (2018) presented chemical evolution with metallicity-dependent weighted rotational velocities by Chieffi & Limongi (2013), but because they adopt the yields of Woosley & Weaver (1995), the evolution of Mg is not well reproduced. Kobayashi et al. (2020), who use the coalescences for massive stars from Kobayashi & Nakasato (2011) and in the presence of failed SNe, were able to reproduce the [Mg/Fe] versus [Fe/H] in the solar neighbourhood. Côté et al. (2017), studying the chemical evolution of Sculptor using the NuGrid stellar yields (Ritter et al. 2018), highlighted that the model results underestimated the observed [Mg/Fe] versus [Fe/H] relation.

In order to be consistent with François et al. (2004) prescriptions, the initial stellar mass function (IMF) formalised by Scalo (1986) is adopted and is assumed to be constant in time and space. More recent IMF formulations were assumed in the chemical evolution models of Kobayashi et al. (2020) (Kroupa 2008, IMF) and Prantzos et al. (2018) (Kroupa 2002, IMF), but the high-mass end is still highly uncertain and affected by large systematic uncertainty (also due to the binary fraction).

A Bayesian framework based on MCMC methods[2] was used in ES21 to fit the APOGEE DR16 chemical abundance ratios at different Galactocentric distances, whereas models in ES20 were constrained by both chemical abundances and stellar ages (APOKASC sample). In both cases, the free parameters of the model were the infall timescales t_1 and t_2, the present-day total surface mass density ratio σ_2/σ_1 between the low- and high-α sequences, and the delay $t_{\max}$. More details on these parameters are provided in Sects. 3.1 and 3.2.

3.1. The reference model from ES20

In ES20, the presented chemical evolution models have been designed to fit the observed chemical abundance ratios and asteroseismic ages of the APOKASC stars (Silva Aguirre et al. 2018). This sample had about 1200 red giants from an annular region with a width of 2 kpc in the solar vicinity. The stellar properties for this sample were determined by fitting the photometric, spectroscopic, and asteroseismic observables using the BAyesian STellar Algorithm code (`BASTA`; Silva Aguirre et al. 2015, 2017; Aguirre Børsen-Koch et al. 2022). In Table 1, we report the best-fit model parameters as predicted by the MCMC calculation performed with $\nu_1 = 2\,\mathrm{Gyr}^{-1}$ and $\nu_2 = 1\,\mathrm{Gyr}^{-1}$ (case *M2* in their paper). In agreement with the classical two-infall model by Chiappini et al. (1997), the first gas infall is characterised by a short period of accretion ($t_1 << t_2$). Furthermore, we notice the presence of a significant delay $t_{\max}$ between the two infall accretion episodes (~4.6 Gyr), as originally found by Spitoni et al. (2019b) but without a quantitative analysis for parameter estimation. An additional observational evidence supporting this scenario was presented by Nissen et al. (2020) who analysed the High Accuracy Radial velocity Planet Searcher (HARPS) spectra of local solar twin stars. These authors found that the age–metallicity distribution shows the presence of two diverse populations characterised by a clear age separation. The authors suggested that these two sequences may be interpreted as evidence of two episodes of accretion of gas onto the Galactic disc with quenching of star formation in between them.

[2] The affine invariant MCMC ensemble sampler code, "*emcee*: the mcmc hammer", developed by Goodman & Weare (2010), Foreman-Mackey et al. (2013) was used to sample the posterior probability distribution.

Table 1. Summary of the main parameters of ES21 (computed at 8 kpc) and ES20 (case *M2*) models.

	Models	
	ES20	ES21
t_1 [Gyr]	$1.264^{+0.119}_{-0.090}$	$0.103^{+0.007}_{-0.006}$
t_2 [Gyr]	$11.282^{+0.954}_{-0.943}$	$4.110^{+0.145}_{-0.127}$
σ_2/σ_1	$4.176^{+0.167}_{-0.178}$	$5.635^{+0.214}_{-0.162}$
$t_{\max}$ [Gyr]	$4.624^{+0.135}_{-0.099}$	$4.085^{+0.021}_{-0.032}$

Notes. We show the best-fit accretion timescales (t_1 and t_2), the present-day total surface mass density ratio (σ_2/σ_1), and delay $t_{\max}$ predicted by the MCMC calculations.

3.2. The reference model from ES21

ES21 presented a multi-zone two-infall chemical evolution model with quantitatively inferred free parameters by fitting the APOGEE DR16 (Ahumada et al. 2020) abundance ratios at different Galactocentric distances. In particular, the model computed at 8 kpc was constrained by the [Mg/Fe] and [Fe/H] ratios of about 9200 stars located in the annular region enclosed between 6 and 10 kpc and vertical height $|z| < 1$ kpc. A significant difference between this model and that of ES20 emerges from Table 1; the ES21 model predicts shorter timescales t_1 and t_2 compared to the ES20 model. This is due to the fact that stellar ages from asteroseismology were not available for constraining the chemical evolution models in the case of ES21. The predicted present-day total surface mass density ratio between the low- and high-α sequences of $\sigma_2/\sigma_1 = 5.635^{+0.214}_{-0.162}$ is in very good agreement with the value derived by Fuhrmann et al. (2017) for the local mass density ratio of 5.26. The presence of an important delay $t_{\max}$ is also confirmed in this case as shown in Table 1. In addition, the model reproduces important observational constraints of the whole Galactic disc, such as the present-day [Mg/H] abundance gradient, the profiles of the SFR, and radial distributions of stellar and gas surface densities (see Sect. 4.3 of Spitoni et al. 2021 for a discussion on the global properties of the Galactic disc reproduced by the ES21 model).

4. Stellar orbital properties: the vertical action, J_z, and the maximum vertical height, $|z_{\max}|$

First, in Sect. 4.1, we briefly recall the relation between the average vertical action and the stellar ages proposed by Ting & Rix (2019). In Sect. 4.2, we discuss the conservation of the vertical action in steady-state potentials and in 'real' late-type galaxies. Finally, in Sect. 4.3, we compute the maximum vertical excursion $|z_{\max}|$ from the Galactic midplane $|z_{\max}|$ as a function of the stellar ages using both the Ting & Rix (2019) relation and the conservation of the vertical action.

4.1. Ting & Rix (2019) relation for the solar vicinity

The action-angle variables are useful quantities for describing the evolution of stellar orbits in steady-state potentials. In particular, here we are interested in the vertical action J_z, defined as:

$$J_z \equiv \frac{1}{2\pi}\int \mathrm{d}z\, \mathrm{d}v_z = \frac{1}{2\pi}\oint \mathrm{d}z\, v_z, \tag{2}$$

where z and v_z indicate the vertical height and velocity along the orbit, respectively. The vertical action therefore quantifies the movement along the z direction of the orbit of a star. These actions are integrals of motion, and therefore in a static, axis-symmetric potential, they are conserved quantities (see the discussion in following section). Ting & Rix (2019) presented a parametric model for the variation of vertical action J_z distribution (i.e. global vertical temperature) analysing the subsample of APOGEE red clump stars in the Galactic disc (Ting et al. 2018) with proper motions from the *Gaia* DR2 (Gaia Collaboration 2018). In Ting & Rix (2019), ages were computed, establishing an empirical, high-dimensional mapping from the APOGEE normalised spectra to stellar ages via a fully connected neural network.

Because red clump stars are strongly biased against stars older than 8 Gyr, Ting & Rix (2019) considered only thin-disc stars younger than 8 Gyr in their model. These authors claimed the existence of a neat relation between vertical action and stellar age, that is, J_z versus τ. Ting & Rix (2019) interpreted the distribution of vertical action as a combination of the vertical action at birth (i.e. vertical birth temperature), which characterised stars when formed out of the Galactic disc, and the subsequent heating (defined as an increase in J_z). This relation computed at the solar radius can be written as

$$\widehat{J_z}(R_\odot, \tau) = 0.91 + 1.81 \cdot \left(\frac{\tau}{1\,\mathrm{Gyr}}\right)^{1.09} \quad [\mathrm{kpc\ km\ s^{-1}}], \tag{3}$$

where on the right side the factor 0.91 is associated with vertical birth temperature, and the second term indicates the age dependence of the vertical action (after birth) which follows a power law of exponent ∼1. In Eq. (3), we label the vertical action with $\widehat{J_z}$ instead of J_z to stress that the proposed model is designed to fit the global observed relation for stellar age and should not be interpreted as the temporal evolution of the vertical action J_z of a single stellar population.

This relation suggests that the vertical heating of all stellar populations is dominated by orbit scattering but the scattering amplitude varies with the Galactic epoch. Ting & Rix (2019) showed that a model with an exponential decrease in the SFR and an inside-out growth of the stellar disc can reproduce the range of power-law indices.

4.2. Conservation of the vertical action J_z for Galactic disc stars

The existence of a non-classical integral of motion associated with the actions of the system, including the vertical action J_z, was discussed at length by Binney & Spergel (1984). Moreover, in the presence of a Galactic potential that changes slowly with time, the vertical action can be considered as an adiabatic invariant. For instance, the cylindrical adiabatic approximation was introduced by Binney (2010) to describe the distribution of stars in the Galactic disc. The author argued that, as the vertical frequency of a disc star is significantly larger than its radial frequency, the potential that affects vertical oscillations may be considered to vary slowly as the star oscillates radially, and consequently J_z is adiabatically invariant. Hence, if the vertical action J_z is an adiabatic invariant, it can also be considered as an approximate invariant under radial migration through churning (Carlberg 1987; Sellwood 2013). For this reason, it seems appropriate to characterise the vertical motions of stars by their vertical actions, J_z, rather than their vertical velocities v_z or velocity dispersion σ_z (we note that σ_z will change in a growing potential and under radial migration).

In principle, external spiral galaxies, which are characterised by high frequency of vertical motion compared to in-plane evolution, should be the perfect candidates where vertical action J_z is a conserved quantity. However, Solway et al. (2012) showed that, for isolated galaxies, the vertical action is not a constant of motion of individual stars, and is only conserved on average for a sample of stars, with an intrinsic dispersion of ∼20%. Furthermore, Vera-Ciro & D'Onghia (2016) used high-resolution N-body simulations of Milky Way-like discs to show that stars deviate from near-circular orbits, reducing the degree to which the actions are conserved for individual stars.

Bearing in mind all of the above-mentioned caveats for late-type galactic systems the in presence of spiral arms like the Milky Way, in the following section we compute orbits for Galactic disc SSPs born at different times, considering the vertical action as a conserved quantity for coeval stars.

4.3. Computing the orbital maximum vertical excursion and the vertical [Mg/Fe] gradient

We assume the three-component steady-state `MWPotential2014` gravitational potential of Bovy (2015) for the Galaxy. The potential model consists of: (i) a bulge modelled as a power-law density profile that is exponentially cut-off; (ii) a Miyamoto-Nagai (Miyamoto & Nagai 1975) disc; and (iii) a dark-matter halo described by the Navarro, Frenk, and White (NFW, Navarro et al. 1996) profile. All parameters and properties of `MWPotential2014` potential are listed in the Table 1 of Bovy (2015). Following the discussion in Sect. 4.2, we impose that each SSP born at 8 kpc in the Galactic plane and initial vertical height coordinate $z = 0$ kpc at a certain Galactic evolutionary time t_B conserves the average vertical action $\widehat{J_z}$ in their orbit subject to the gravitational potential of the Galaxy.

In the calculations, we consider SSPs formed in constant age intervals $\Delta\tau$ fixed at the value of 0.005 Gyr (the total number of SSPs is 2740), which is identical to the time-step of the chemical evolution model. Recalling the Ting & Rix (2019) relation introduced in Sect. 4.1 and the associated discussion, the value of conserved vertical action $\widehat{J_z}$ for a SSP with age $\tau = t_G - t_B$ can be estimated using Eq. (3), where t_G is the age of the Galaxy.

We integrate stellar orbits for different SSPs(τ) using the GALPY[3] package subject to the `MWPotential2014` gravitational potential (Bovy 2015). For the rotational velocity v_T at the solar distance $R_\odot$, we use the one computed by Ablimit et al. (2020), applying the three-dimensional velocity vector method for Cepheids ($v_T = 232.5 \pm 0.83$ km s^{-1}) that is consistent with the most recent estimation by Nitschai et al. (2021) with a dynamical model of the Milky Way using APOGEE and *Gaia* data. The initial vertical velocity for the SSP $v_{0,z}(\tau)$ born at the evolutionary time $t_B = t_G - \tau$ was chosen by satisfying the

[3] http://github.com/jobovy/galpy

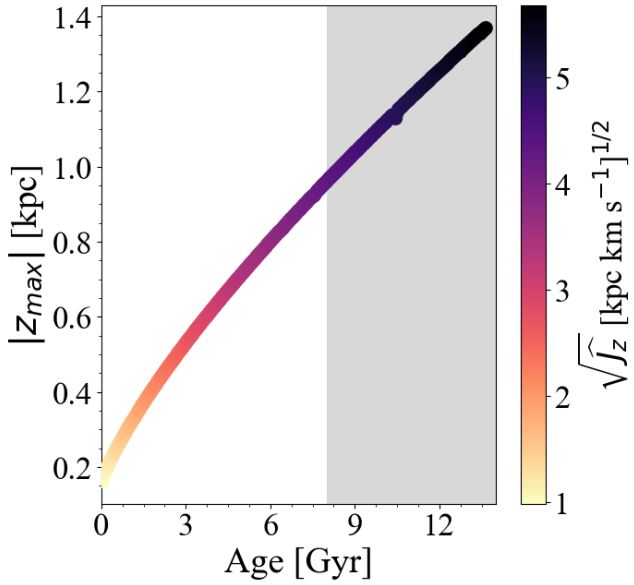

Fig. 2. Maximum vertical excursion $|z_{\max}|$ predicted for sequential SSPs born at 8 kpc at different Galactic evolutionary times as a function of their age, adopting Eq. (3) and imposing the conservation of J_z in the orbital integration (see Sect. 4.3). The colour coding indicates the values of the $\sqrt{J_z}$ quantity. We note that Eq. (3) was retrieved for thin disc stars in the solar vicinity for APOGEE stars younger than 8 Gyr. The shaded region shows SSPs that are older than 8 Gyr, for which the use of Eq. (3) may not be justified.

following condition:

$$\Big| \underbrace{J_z\big(R_\odot, v_{0,z}(\tau)\big)}_{\text{GALPY}} - \underbrace{\widehat{J_z}(R_\odot, \tau)}_{\text{Ting \& Rix (2019)}} \Big| < 0.05\ [\text{kpc km s}^{-1}], \quad (4)$$

where the computed vertical action J_z with GALPY and that with Eq. (3) differ by less than 0.05 [kpc km s^{-1}]. In Fig. 2, we show the maximum vertical excursion from the midplane $|z_{\max}|$ as a function of the SSP age and vertical action with an age resolution of $\Delta\tau = 0.05$ Gyr, assuming that the initial vertical height is $z = 0$ kpc at any Galactic time (all the stars are born exactly on the disc plane).

One of the most important conclusions of Ting & Rix (2019) is that orbital scattering is a plausible and viable mechanism to explain the age-dependent vertical motions of disc stars. Hence, here we assume that the star formation happens in the disc plane with null vertical height ($z = 0$ kpc) where the infalling gas gets accreted (see Eq. (1)). Higher vertical coordinates $|z_{\max}|$ (see Fig. 2) can be reached only by older SSPs because of the kinematic scattering. Here, we are ignoring the extra-heating processes from merging events in which stars from galactic systems are engulfed by the Galaxy (Helmi et al. 2018).

In Fig. 3, we show the initial vertical velocities $v_{0,z}(\tau)$ as a function of Galactic age for the SSPs born at different evolutionary times $t_B = t_G - \tau$. In the presence of the steady-state gravitational potential `MWPotential2014`, the initial vertical velocity of one SSP formed in the Galactic plane (with initial vertical height $z = 0$ kpc) in the solar neighbourhood also corresponds to the maximum vertical velocity of the orbit. In Fig. 3, we also show the temporal evolution of the modulus of the vertical velocity component of the SSP born in the Galactic plane ($z = 0$ kpc) at 8 kpc at the Galactic time $t_B = t_G - 1$ Gyr and integrated for 1 Gyr. It is evident that the vertical velocity at the

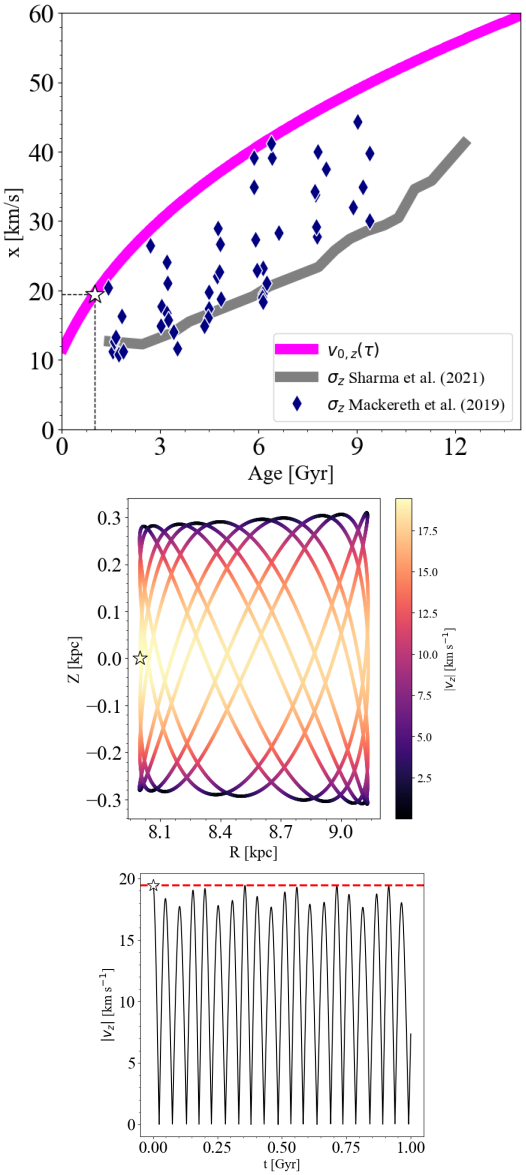

Fig. 3. The connection between the initial vertical velocity $v_{0,z}(\tau)$ and the velocity dispersion σ_z. *Upper panel:* computed initial vertical velocity $v_{0,z}(\tau)$ (which satisfies the condition of Eq. (4)) as a function of Galactic age τ for the SSPs born at different evolutionary times shown as the solid magenta line. Data for the age–velocity dispersion σ_z relation in the solar vicinity from Sharma et al. (2021) and Mackereth et al. (2019) are drawn with the grey line and diamond blue points, respectively. *Middle panel:* orbit in the meridional plane (R, Z) for the SSP born in the Galactic plane ($z = 0$ kpc) at 8 kpc (labelled with a star) at the Galactic time $t_B = t_G - 1$ Gyr and integrated for 1 Gyr. The colour-coding stands for the modulus of the vertical velocity component $|v_z|$. *Lower panel:* the 1 Gyr evolution of the modulus of the vertical velocity component $|v_z|$ for the same SSP as the lower left panel. The starred symbol indicates the vertical velocity associated at birth $v_{0,z}(\tau = 1\,\text{Gyr})$ (also indicated in the other panels with the same symbol) which also corresponds to the maximum value of the vertical velocity component $|v_z|$ (see red dashed horizontal line).

SSP birth $v_{0,z}(\tau = 1\,\text{Gyr})$ corresponds to the maximum value of the modulus of vertical velocity $|v_z|$.

Because of the symmetry of the system, we can consider this quantity as an estimate for the upper limit of the vertical velocity dispersion σ_z at the Galactic age τ. Hence, considering all

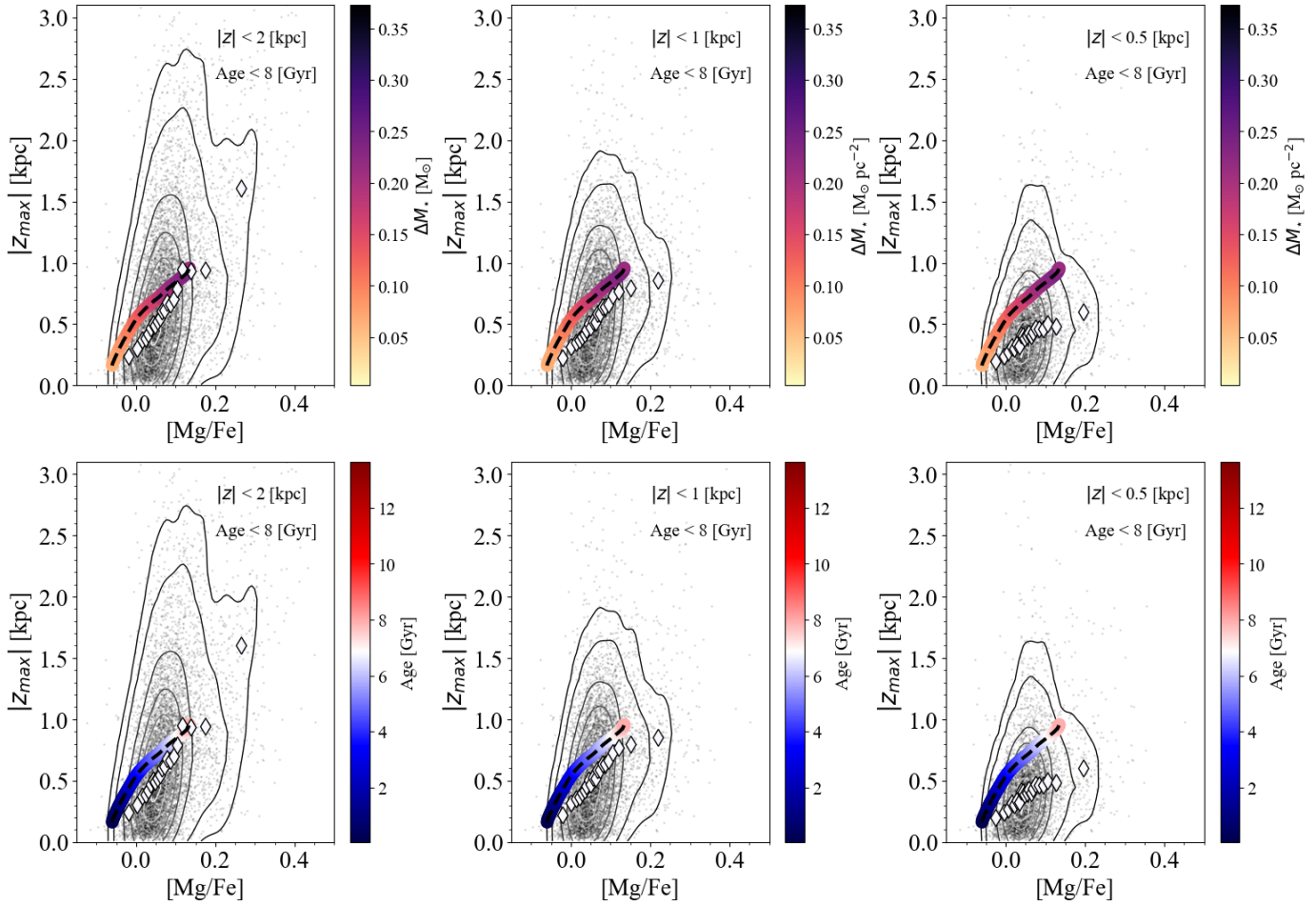

Fig. 4. The study of the [Mg/Fe] versus $|z_{\rm max}|$ relation with stellar ages <8 Gyr. The grey points indicate stars with observed [Mg/Fe] abundance ratios for stars from APOGEE DR16 (Ahumada et al. 2020) in the Galactocentric region between 6 and 10 kpc as a function of the computed maximum vertical heights $|z_{\rm max}|$ with ages <8 Gyr as reported in the astroNN catalogue. White diamonds stand for the median $|z_{\rm max}|$ and [Mg/Fe] values in bins of [Mg/Fe] with the same number of stars. The contour lines enclose fractions of 0.95, 0.90, 0.75, 0.60, 0.45, 0.30, 0.20, and 0.05 of the total number of observed stars. Stars with observed vertical heights of $|z| < 2$ kpc, $|z| < 1$ kpc, and $|z| < 0.5$ kpc are reported in the *left, middle, and right panels*, respectively. ES21 only model predictions for stars younger than 8 Gyr, including the J_z versus age relation by Ting & Rix (2019), which is indicated in each panel with the dashed black line. In the *upper panels*, the colour coding indicates the predicted surface stellar mass density $\Delta M_\star$ formed in age intervals of 0.05 Gyr. In *lower panels*, the colour-coded circles depict ages of new SSPs formed during the Galactic evolution in age intervals of 0.05 Gyr. Although the upper limit for the maximum vertical $|z_{\rm max}|$ in all panels has been fixed at a value of 3 kpc, excluding outlier stars, the median values and the contour density lines have been computed taking into account all the stars in the respective samples.

the SSPs born at different evolutionary times, we can estimate the upper limit of the observed vertical velocity dispersion σ_z versus Galactic age τ relation. In Fig. 3, we compare the predicted $v_{0,z}(\tau)$ values with the age–σ_z relations observed in the solar vicinity by Mackereth et al. (2019) who analyse APOGEE stars and by Sharma et al. (2021) for GALAH objects. In Fig. 3, each Mackereth et al. (2019) data point represents one mono–[Fe/H] bin, which contains more than 200 stars. We note that the computed initial velocity distribution accurately traces the upper limit of the age–σ_z relation.

As mentioned in Sect. 1, the ES21 model predicts that the Galactic disc follows an inside-out formation and consequently the Galactic potential should evolve as a function of time as well. In the Milky Way-like galaxy in the cosmological context presented by Bird et al. (2013) and characterised by an inside-out formation, the surface stellar mass density and the median height above the disc (of stellar populations born at different Galactic ages) did not vary considerably in the last ∼8 Gyr at the solar distance. This implies that the inside-out formation did not substantially affect the Galactic potential at Galactic ages <8 Gyr. A static potential for the integration of the orbit of stars with ages <8 Gyr (see Fig. 4) is therefore a valid approximation. However, this may not be true when we extend the Ting & Rix (2019) relation to older ages; it is important to stress this caveat of our approach.

In the following section, we show model predictions combining the [Mg/Fe] abundance ratio for stars born at different Galactic times (i.e. with different ages τ) as predicted with chemical evolution models presented in Sect. 3 with the maximum orbital height above the plane $|z_{\rm max}|(\tau)$ computed as described in Sect. 4.3.

5. Results

We compare the vertical [Mg/Fe] abundance distribution in the solar vicinity predicted by chemical evolution models presented in Sect. 3 to the observed APOGEE DR16 stellar abundance ratios and the associated orbital properties and ages as presented

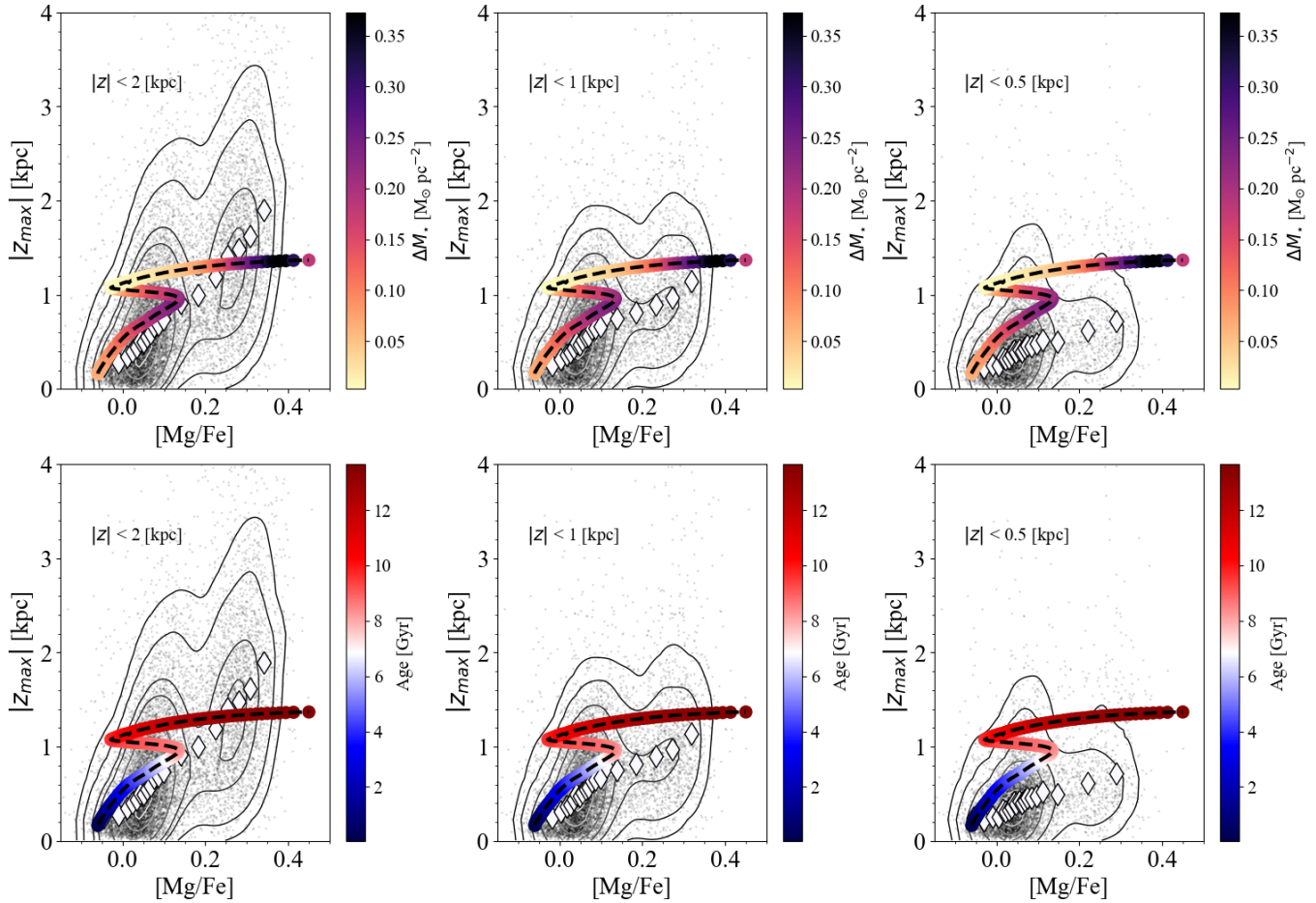

Fig. 5. Same as Fig. 4, but observed and predicted stars older than 8 Gyr have also been depicted, extending the Ting & Rix (2019) relation to all stellar ages (see Fig. 2). In the figure, the maximum vertical height is shown between 0 and 4 kpc for the sake of clarity, but the median values and the contour density lines were computed using all stars (including those with $|z_{\rm max}|$ greater than 4 kpc).

in the astroNN catalogue (see Sect. 2). We show results for the case where all stars are younger than 8 Gyr and also for the case where all ages are included. We recall that the Ting & Rix (2019) relation for the vertical action (Eq. (3)) was recovered for stars younger than 8 Gyr (thin disc stars). Here, we test whether extending this relation to older stellar populations allows us to reproduce the vertical distribution of the [Mg/Fe] abundances in APOGEE data for the full age range.

5.1. ES21 model

In Fig. 4, we show vertical abundance distributions using the ES21 model computed at 8 kpc as expressed by the relation between the maximum vertical height $|z_{\rm max}|$ (see the methodology in Sect. 4.3) and the [Mg/Fe] abundance ratios for stars with ages <8 Gyr. We considered different cuts in the observed Galactic vertical heights, that is, $|z| < 2$ kpc, $|z| < 1$ kpc, and $|z| < 0.5$ kpc, in order to better analyse the vertical structure.

Observed stars with astroNN ages of younger than 8 Gyr are more likely part of the low-α sequence. Moreover, the vertical [Mg/Fe] abundance gradient seems to be traced by a single stellar sequence as visible from the contour density lines: the contour which encloses 75% of the stars is absent of any elongated structure towards higher [Mg/Fe] values and therefore shows no trace of bimodality.

In Fig. 4, we note that the observed $|z_{\rm max}|$ versus [Mg/Fe] relations traced by stars with observed vertical heights $|z| < 2$ (left panels) and $|z| < 1$ kpc (middle panels) are well reproduced by our model predictions. In contrast, smaller $|z_{\rm max}|$ values than the computed one emerge from the data in the right panel with $|z| < 0.5$ kpc: in this case, a consistent number of observed low-α stars were discarded.

In our model computed in the solar neighbourhood, an age of less than 8 Gyr corresponds to an evolutionary time of more than 5.7 Gyr. In ES21, the quantity $t_{\rm max}$ (i.e. the delay between the two peaks of gas infall) is 4.085 Gyr (see Table 1). Therefore, when considering only stars with ages <8 Gyr, we exclude some thin disc stars, specifically the ones formed soon after the beginning of the second gas infall (born at an evolutionary time of between 4.085 and 5.7 Gyr), and totally ignoring the thick-disc component.

In Fig. 5, we show model results extending the Ting & Rix (2019) relation to high-α sequence stars (ages >8 Gyr, i.e. the grey shaded area in Fig. 2). The stellar sample with the full age range of the astroNN catalogue shows a clear bimodality in the $|z_{\rm max}|$ versus [Mg/Fe] relation, which is more evident with the cut $|z| < 2$ kpc (left panels in Fig. 5). Our model is able to predict such a dichotomy, displaying two different sequences in the $|z_{\rm max}|$ versus [Mg/Fe] relation. In the phase when the star formation resumes immediately after the beginning of the second gas infall, ejecta from Type II SNe produce a steep rise in the [α/Fe]

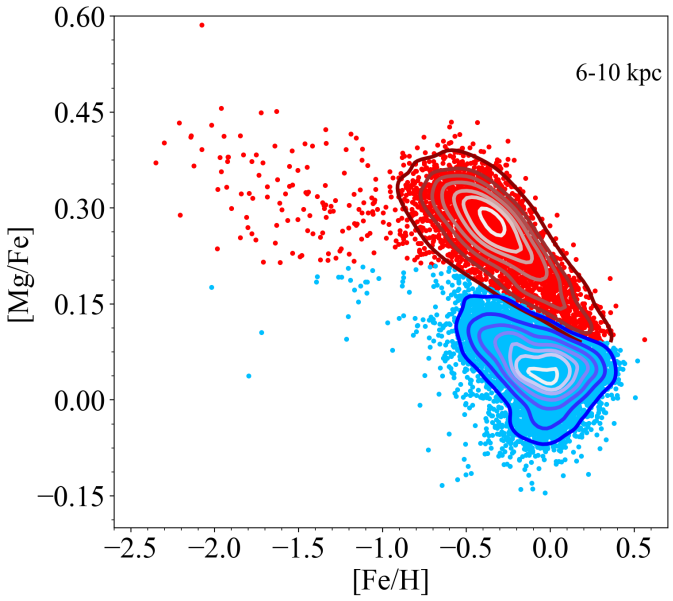

Fig. 6. Disc components selected based on the chemistry of the APOGEE stars in the Galactic region enclosed between 6 and 10 kpc presented in Sect. 2. Red points show high-α sequence stars, and light blue points show the low-α ones. The contour lines enclose fractions of 0.95, 0.90, 0.75, 0.60, 0.45, 0.30, 0.20, and 0.05 of the total number of observed stars for the two sequences, separately.

ratio followed by a decrease due to pollution from Type Ia SNe as visible in Fig. 5. This kind of transition between the two disc sequences is not obvious in the data. However, as pointed out by the colour-coded points indicating the stellar mass $\Delta M_\star$ produced in the constant age interval of $\Delta\tau = 0.05$ Gyr, the 'upturning' feature in the chemical evolution track is characterised by low stellar-mass content compared to other Galactic evolutionary phases.

In Fig. 5, we see that the predicted curve for the vertical [Mg/Fe] distribution by the model nicely overlaps with the regions with the highest densities of stars in both low-α and high-α APOGEE stars with observed heights $|z| < 2$ kpc (left panels). However, the observed median $|z_{\rm max}|$ values (computed in bins of [Mg/Fe] with the same number of stars) for high-α stars are larger than our model results. In fact, we predict an overly flat (almost constant) growth of the maximum vertical height $|z_{\rm max}|$ for thick-disc sequence stars.

One possible explanation for such a discrepancy is that the stellar sample is contaminated by the presence of halo stars. However, it is more likely that other dynamical processes, such as merger and accretion episodes, have played a crucial role in perturbing stellar orbits of the high-α sequence in addition to simple scattering processes as assumed by the Ting & Rix (2019) model for thin-disc stars (stellar ages <8 Gyr). Cosmological simulations have shown that Milky Way-like galaxies frequently experience minor mergers (Quinn et al. 1993; Walker et al. 1996; Velazquez & White 1999; Kazantzidis et al. 2009; House et al. 2011; Gómez et al. 2013; D'Onghia et al. 2016; Moetazedian & Just 2016), external perturbations that can heat up the disc. Helmi et al. (2018) demonstrated that the inner halo is dominated by debris from an accreted object more massive than the Small Magellanic Cloud, alias *Gaia*-Enceladus (Vincenzo et al. 2019). *Gaia*-Enceladus must have led to dynamical heating of the precursor of the Galactic thick disc (stars with the same [α/Fe] versus [Fe/H] as thick disc but with different kinematics). Moreover, radial stellar migration (Sellwood & Binney 2002; Schönrich & Binney 2009; Minchev & Famaey 2010) should cause more extended vertical motion at reduced velocity dispersion for stars that move outward, and the opposite effect for stars that move inward (Loebman et al. 2011; Minchev et al. 2012).

In Fig. 5, we note that the median values of the observed vertical [Mg/Fe] distribution for $|z| < 1$ kpc (middle panels) and $|z| < 0.5$ kpc cases (right panels) show an evident change in the slope as we move from low-α (steeper) to high-α stars (flatter), which is more in agreement with our model predictions compared with the $|z| < 2$ kpc cut (left panels). Hence, it is likely that by applying $|z| < 1$ kpc and $|z| < 0.5$ kpc cuts, we are excluding objects from the APOGEE sample that have possibly been affected by extra heating from past merging events.

We conclude that, if we consider the objects with $|z| < 2$ kpc as high-α sequence stars, some extra heating from gravitational perturbers (i.e. the constellation of clusters, small dwarf galaxies) should be taken into account to achieve better agreement between model results and observed $|z_{\rm max}|$ versus [Mg/Fe] median values. Recently, Conroy et al. (2021) showed that the Large Magellanic Cloud (LMC) has an impact on the position of the centre of mass of the Milky Way + LMC system, and creates important dynamical signatures in the MW (and LMC) halo as well.

In order to further investigate the validity of the proposed two-infall model, we compare the observed and predicted $|z_{\rm max}|$ distributions (studying only the case with $|z| < 2$ kpc because of the evident bimodality in the [Mg/Fe] versus $|z_{\rm max}|$ space) assuming a separation between high-α and low-α stars based on chemistry. In Fig. 6, we report the APOGEE-DR16 stars with the same selection criteria as presented in Sect. 2, where we impose a disc dissection based on chemistry similar to the one suggested by Silva Aguirre et al. (2018) for the APOKASC sample and by Ness et al. (2019).

In the first row of Fig. 7, we compare $|z_{\rm max}|$ distributions predicted by the ES21 model with data for the whole stellar sample (left panel), high-α sequence stars (middle panel), and low-α sequence stars (right panel), respectively. Following the same procedure adopted in Spitoni et al. (2019b), we assume that SSPs formed at evolutionary times smaller (larger) than $t_{\rm max}$ (which is time-delay between the two gas infall events) are considered as part of the high(low)-α sequence. As in Fig. 5 for the $|z_{\rm max}|$ versus [Mg/Fe] distributions, here we are primarily interested in reproducing the trend of the observations. Indeed, in Fig. 7, the predicted median values by the ES21 model are consistent with the APOGEE DR16+astroNN catalogue stars. However, we notice that we fail in reproducing the large spread of the observed distribution, especially for the high-α case.

Gandhi & Ness (2019), studying the stellar dynamics for LAMOST stars with distances of less than 2 kpc from the Sun, found a large dispersion in the computed vertical action J_z versus age relation; that is, for the high-α sequence they find $\sigma_{J_z}/J_z = 0.9$ and $\sigma_{J_z}/J_z = 1.13$ for low-α stars. Similar results were found by Ting & Rix (2019).

We take into account this dispersion in our model by adding, at each Galactic time t, a random error which has a Gaussian distribution to the vertical action $\widehat{J_z}$ of Ting & Rix (2019) associated to the SSP formed at Galactic time t.

The 'new' vertical action $\widehat{J_{z,\rm new}}(t)$ is defined as

$$\widehat{J_{z,\rm new}}(t) = \widehat{J_z}(t) + \delta_G(\widehat{J_z}(t)); \; \delta_G(t) \sim \mathcal{N}(0, \sigma_{J_z}), \tag{5}$$

where δ_G is a perturbation that follows a normal distribution $\mathcal{N}(0, \sigma_{J_z})$ with standard deviation σ_{J_z}. In conclusion, we

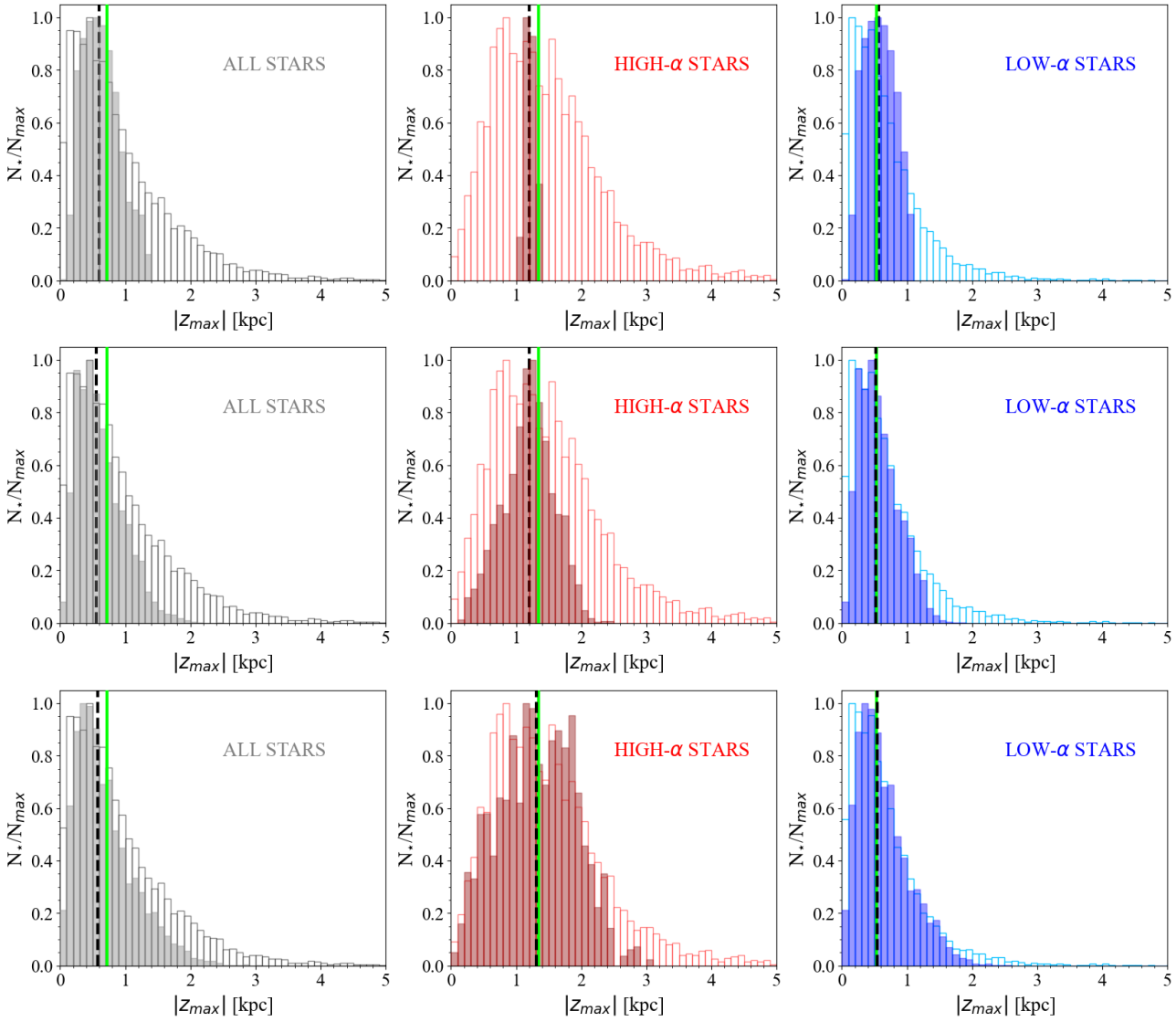

Fig. 7. Comparison between the predicted $|z_{\rm max}|$ distributions by the ES21 model (filled histograms) with APOGEE+astroNN stars (empty histograms) for the whole stellar sample introduced in Sect. 2 (*left panels*), for the high-α sequence (*middle panels*), and for the low-α sequence (*right panels*) normalised to the maximum number of stars in the bins of the distributions. In the first row we report ES21 predictions using the vertical action J_z reported in Eq. (3) without including any errors. In the second row, we report ES21 model results, adding a random error normally distributed around J_z with standard deviation σ_{J_z} fixed at the values of $\sigma_{J_z} = 0.5 \cdot J_z$. Finally, in the last row the case with $\sigma_{J_z} = 1 \cdot J_z$ is drawn. In each panel, the vertical solid green and dashed black lines indicate the median values of APOGEE stars and model predictions, respectively.

perturbed the J_z–age relation of Ting & Rix (2019), and $\widehat{J_{z,\rm new}}$ is taken as the new constraint when we compute J_z with GALPY varying the initial vertical velocity as indicated in Eq. (4).

In the light of results obtained by Gandhi & Ness (2019) and Ting & Rix (2019), in Fig. 8 we show the J_z versus age relations and the initial vertical velocities $v_{0,z}(\tau)$ for the SSPs in the solar neighbourhood with $\sigma_{J_z}/J_z = 0.5$ and $\sigma_{J_z}/J_z = 1$. In Fig. 7, we also show the $|z_{\rm max}|$ distributions with $\sigma_{J_z}/J_z = 0.5$ (second row) and $\sigma_{J_z}/J_z = 1$ (third row). We note that the predicted medians of the $|z_{\rm max}|$ distribution with $\sigma_{J_z}/J_z = 1$ for both the high- and low-α sequences are in good agreement with the data. Moreover, the observed spread of the distribution is satisfactorily reproduced. On the other hand, the $\sigma_{J_z}/J_z = 0.5$ case (as reported in the second row) does not allow our model to mimic the observed spread in the high-α sequence. Moreover, even with $\sigma_{J_z}/J_z = 1$ the high $|z_{\rm max}|$ tail of the distribution (stars with $|z_{\rm max}| > 3$ kpc) cannot be predicted by the model. We think that other sources of error could be the cause of this discrepancy. However, here we want to focus solely on the effects of uncertainties on the J_z determination.

In Fig. 9, we also show the predicted age versus $|z_{\rm max}|$ distributions assuming $\sigma_{J_z}/J_z = 0.5$ (left panel) and $\sigma_{J_z}/J_z = 1$ (right panel) compared to astroNN ages (computed by Mackereth et al. 2019 using a Bayesian neural network model trained on asteroseismic ages). We can see that the trend of observed spread in the $|z_{\rm max}|$ versus age distribution is better reproduced with $\sigma_{J_z}/J_z = 1$. In the lower panels of Fig. 9, we see that the distributions of the predicted SSPs in the $|z_{\rm max}|$ versus [Mg/Fe] space, including the observed dispersion in the vertical action J_z estimates, highlight the presence of the disc dichotomy signature, in agreement with data. It is worth mentioning that in Johnson et al. (2021) radial mixing and the age-velocity relation can explain the dependence of the relative frequency of high- and low-α stars on R and $|z|$.

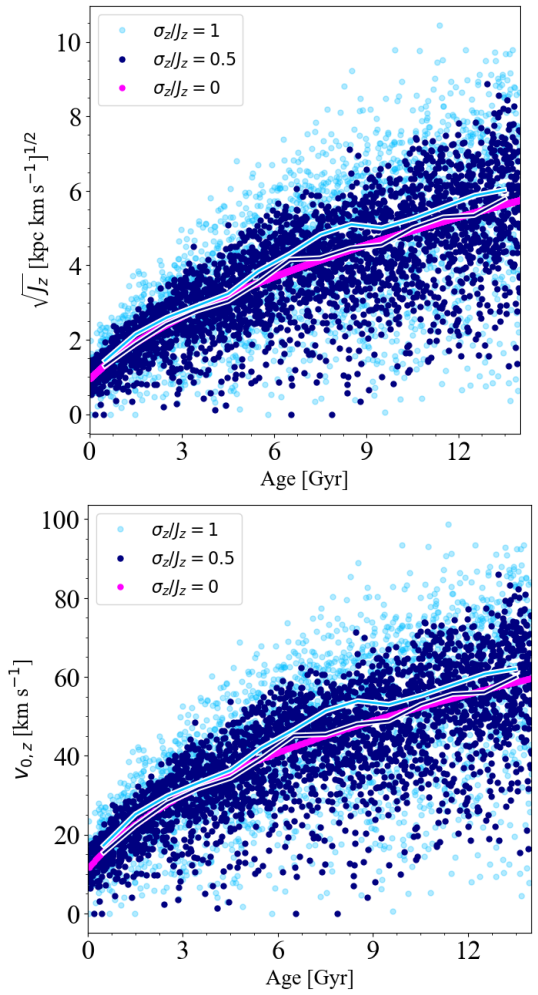

Fig. 8. The inclusion of the dispersion in the vertical action J_z estimates in the Ting & Rix (2019) relation. *Upper panel:* the Ting & Rix (2019) relation between vertical action J_z and stellar age computed at 8 kpc is indicated with the magenta line. The 'new' vertical action $\widehat{J}_{z,\mathrm{new}}$ of Eq. (5) including observed dispersion for $\sigma_{J_z}/J_z = 0.5$ and $\sigma_{J_z}/J_z = 1$ cases is reported with the dark and light-blue points, respectively. The solid dark-blue (light-blue) line indicates the median values for $\sigma_{J_z}/J_z = 0.5$ ($\sigma_{J_z}/J_z = 1$). *Lower panel:* computed initial vertical velocity $v_{0,z}(\tau)$ (which satisfies the condition of Eq. (4)) as a function of Galactic age τ for the SSPs born at different evolutionary times is reported with the solid magenta line. As in the upper panel, the computed $v_{0,z}$ including observed dispersion for $\sigma_{J_z}/J_z = 0.5$ and $\sigma_{J_z}/J_z = 1$ cases is indicated with the dark and light-blue points, respectively.

As already noted in ES21, the predicted distribution of surface stellar mass density $\Delta M_\star$ (computed in constant age intervals fixed at the value of 0.05 Gyr) in the [Mg/Fe] versus [Fe/H] relation is in contrast with the APOGEE DR16 stellar distribution. Also in Fig. 5, the model forms too many stars as soon as the first infall begins, and in the [Mg/Fe] versus $|z_{\mathrm{max}}|$ relation, they populate a region where stars from APOGEE DR16 are rare, that is, [Mg/Fe] with values larger than 0.3 dex. This is due to the fact that the best fit-model parameter value for the infall timescale τ_1 of the high-α sequence is ∼0.1 Gyr, and therefore the bulk of high-α stars are created in a region in the $|z_{\mathrm{max}}|$ versus [Mg/Fe] plane where population density is low in APOGEE DR16. In Sect. 5.2, we show that a longer timescale of gas accretion t_1 in the high-α sequence, which characterised the ES20 model (see Table 1), is able to alleviate this tension.

5.2. ES20 model

In this section, we compare the combined APOGEE data + astroNN catalogue with model predictions based on the chemical evolution model *M2* of ES20. Figure 10 shows model results with the Ting & Rix (2019) relation extended to high-α sequence stars in computing the maximum height $|z_{\mathrm{max}}|$. As for the ES21 model (see Sect. 5.1), better agreement with the data is obtained when APOGEE DR16 stars with observed vertical heights $|z| < 2$ kpc are considered.

As pointed out in Sect. 5.1, there is a discrepancy between the regions in the maximum vertical height versus [Mg/Fe] relation most densely populated by APOGEE DR16 stars and the peaks of the predicted distribution of the stellar mass density found by the ES21 model. On the other hand, in Fig. 10 we note that the distribution of the formed stars predicted by the ES20 model throughout the curve in the $|z_{\mathrm{max}}|$ versus [Mg/Fe] space shows no tension with the data. Indeed, the two peaks of the predicted stellar mass density are in correspondence with the highest data-density regions as traced by the contour density curves. We reiterate that the best-fit parameters in model *M2* of ES20 have been constrained by the APOKASC sample, and take into account stellar age computed with asteroseismology in the MCMC calculations. As discussed in Sect. 3, longer timescales t_1 and t_2 for the gas accretion are predicted by this model constrained by the APOKASC sample (see Table 1). Regarding the high-α sequence, the main consequence of the slower gas accretion is to delay the peak of the star formation towards smaller [Mg/Fe] values.

Figure 11 reports the predicted surface stellar mass density $\Delta M_\star$ formed in age intervals of 0.05 Gyr as a function of the [Mg/Fe] abundance ratio predicted by ES20 and ES21 models, respectively. Here, it is even more evident that in the ES20 model the peak of the stellar mass formed during the high-α sequence phase is shifted towards smaller [Mg/Fe] values.

In Fig. 12, we notice that the distributions of the predicted SSPs in the $|z_{\mathrm{max}}|$ versus [Mg/Fe] space – where the observed dispersion in the vertical action J_z estimates is included in the ES20 model – reveal the presence of the disc dichotomy feature, in good agreement with data.

Finally, Fig. 13 shows that for the ES20 model the median values of the observed $|z_{\mathrm{max}}|$ distributions of APOGEE-DR16+astroNN stars are also well reproduced for both the high- and low- α sequences. However, as already discussed in Sect. 5.1, in order to mimic the observed spread, the model must also include the errors of $\sigma_{J_z} = 1 \cdot J_z$ in the considered vertical action J_z (see the last row of Fig. 13).

5.3. [Mg/Fe] distribution functions and 3D space ([Mg/Fe], [Fe/H], $|z_{\mathrm{max}}|$) analysis

In Sect. 5.1, we point out that the predicted distribution in the $|z_{\mathrm{max}}|$ versus [Mg/Fe] relation by ES21 of the newly formed stellar mass in the same age bins (i.e., $\Delta\tau = 0.05$ Gyr) in the high-α sequence is in contrast with the APOGEE data. On the other hand, this tension is resolved when adopting the ES20 model. In Fig. 14, we compare the [Mg/Fe] distribution function computed by ES21 and ES20 models with the APOGEE DR16 data in the annular Galactic region enclosed between 6 and 10 kpc (for consistency with the distribution reported in Fig. 16 of Spitoni et al. 2021 we consider stars with vertical heights $|z| < 1$ kpc). The ES21 best-fit model (green histogram) accounts for the observed bimodality, but the predicted peaks are significantly shifted towards higher [Mg/Fe] values. As underlined in

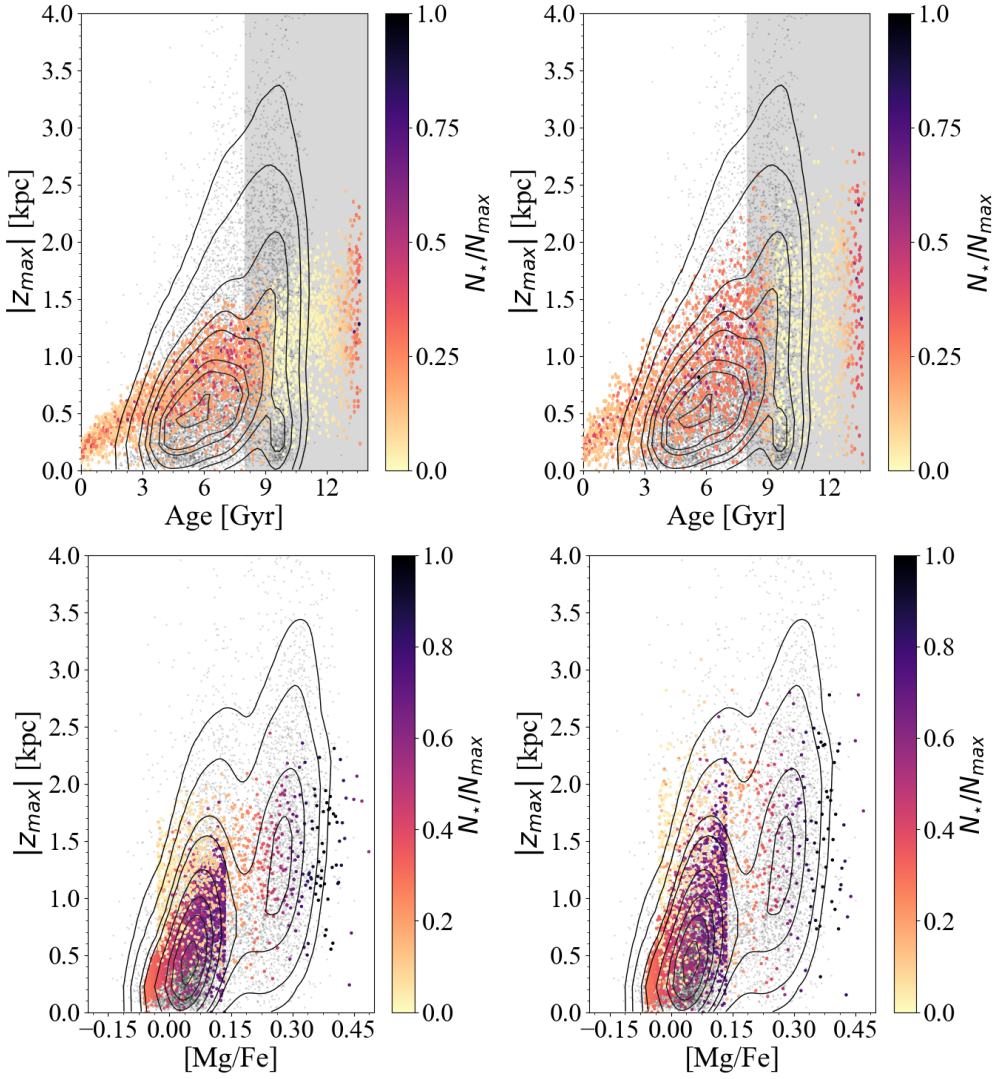

Fig. 9. The inclusion of the dispersion in the vertical action J_z estimates in the Ting & Rix (2019) relation. *Upper panels:* vertical maximum excursion $|z_{\max}|$ versus age relation for the ES21 model. The grey points indicate stars within the Galactocentric region between 6 and 10 kpc and $|z| < 2$ kpc as reported in the astroNN catalogue. The contour lines enclose fractions of 0.95, 0.90, 0.75, 0.60, 0.45, 0.30, 0.20, and 0.05 of the total number of observed stars. The colour coding represents the total number of stars predicted by the ES21 model in that region. In the left panel, we draw model results considering a Gaussian error (see Eq. (5)) with standard deviation $\sigma_{J_z} = 0.5 \cdot J_z$, whereas in the right panel we assume $\sigma_{J_z} = 1 \cdot J_z$. The shaded grey area highlights the region with ages of more than 8 Gyr, for which the use of Eq. (3) may not be justified. *Lower panels:* as in the upper ones, but for the $|z_{\max}|$ versus [Mg/Fe] relations.

Sect. 5.1, this is due to the short timescales of accretion τ_1 and τ_2 as obtained by the MCMC calculation when only chemical APOGEE DR16 abundances are fitted, which cause the star formation activity to be concentrated close to the peaks of maximum gas infall rates. On the contrary, model *M2* by ES20, which is characterised by longer timescales of accretion (see Table 1), predicts the above-mentioned bimodality and is capable of reproducing the [Mg/Fe] values of high-α and low-α distribution peaks as shown in APOGEE DR16 data. We conclude that the inclusion of precise stellar ages inferred from asteroseismology is fundamental in order to properly constrain chemical evolution models of the Milky Way disc components.

Finally, in Fig. 15 we compare model predictions in the 3D space formed by the abundance ratios [Mg/Fe], [Fe/H] and the orbital parameter $|z_{\max}|$ with APOGEE DR16 data (observed Galactic heights $|z| < 2$ kpc). In the left panel of Fig. 15 we analyse the whole stellar age range. Colour-coded points indicating the stellar mass $\Delta M_\star$ formed in age intervals of 0.05 Gyr highlight that in the ES21 model the star formation in the high-α sequence is concentrated towards the infall rate peak (see also Fig. 11), whereas in ES20 it is characterised by a more extended star formation history and as mentioned above the predicted [Mg/Fe] distribution function is in agreement with APOGEE DR16. In the projections, it can be noted that the evident dichotomy present in the data in the plane of $|z_{\max}|$ versus [Mg/Fe] is not as clear in $|z_{\max}|$ versus [Fe/H]. On the right panel of Fig. 15, where we consider only stars younger than 8 Gyr, it is possible to see the good agreement between model predictions and data.

6. Conclusions

Recent chemical evolution models designed to reproduce APOGEE DR16 data (Spitoni et al. 2021) and the APOKASC sample (Spitoni et al. 2020) suggest the presence of a significant delay time between the two gas-infall episodes that lead to

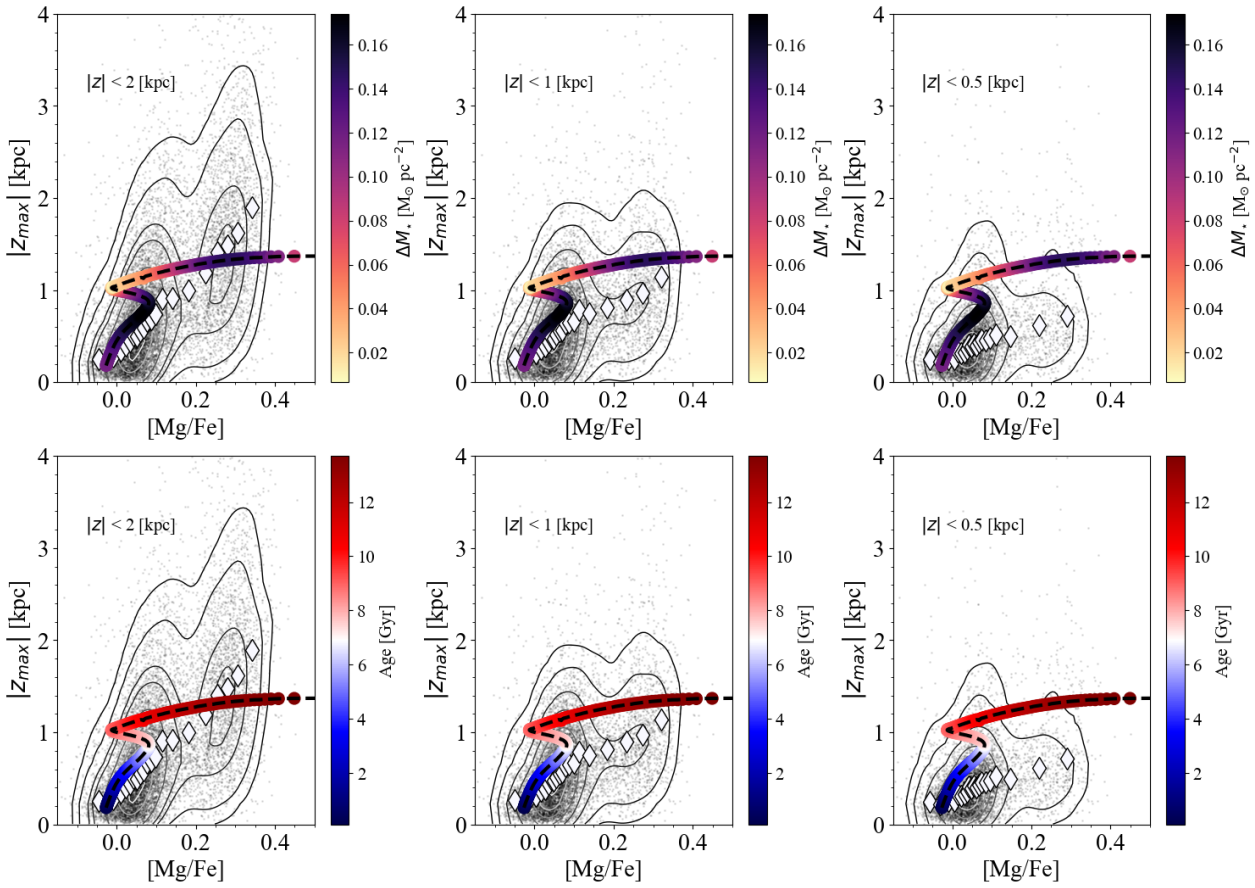

Fig. 10. As in Fig. 5 but considering chemical evolution results of the model *M2* of ES20.

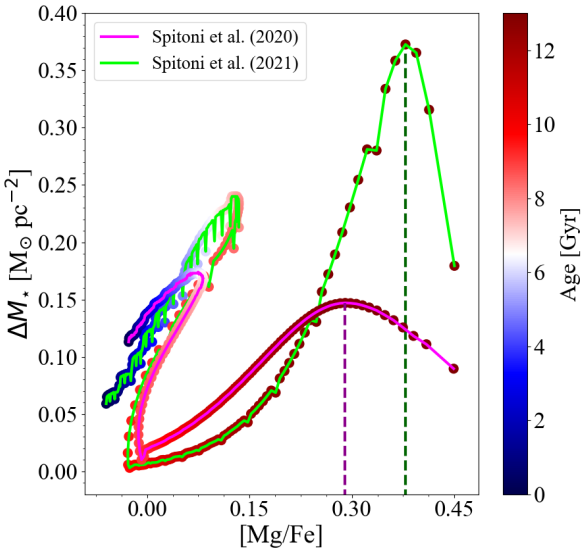

Fig. 11. Predicted surface stellar mass density $\Delta M_\star$ formed in age intervals of 0.05 Gyr as a function of the [Mg/Fe] abundance ratio predicted by the ES21 model (green solid line) and by the *M2* model of ES20 (magenta solid line). Colour-coded points correspond to different ages of the SSPs. Vertical dashed lines depict the associated maximum $\Delta M_\star$ values in the high-α sequence stars.

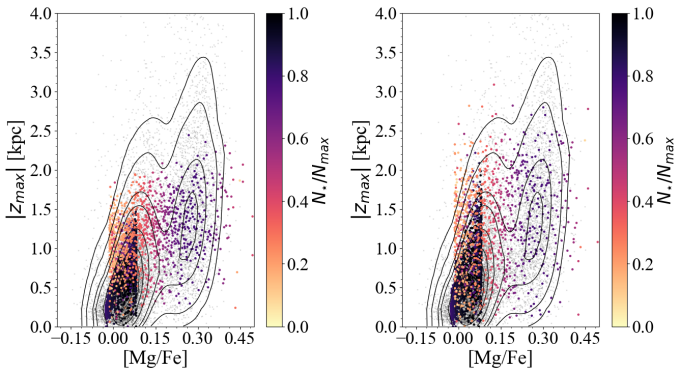

Fig. 12. Vertical maximum excursion $|z_{\rm max}|$ versus [Mg/Fe] relation for the ES20 model. The grey points indicate stars within the Galactocentric region between 6 and 10 kpc and $|z| < 2$ kpc as reported in the astroNN catalogue. The contour lines enclose fractions of 0.95, 0.90, 0.75, 0.60, 0.45, 0.30, 0.20, and 0.05 of the total number of observed stars. The colour coding represents the total number of stars predicted by the ES21 model in that region. In the left panel, we draw model results considering a Gaussian error (see Eq. (5)) with standard deviation $\sigma_{J_z} = 0.5 \cdot J_z$, whereas in the right one we assume $\sigma_{J_z} = 1 \cdot J_z$.

formation of the thick disc and the thin disc. In this work, we present results for the vertical distribution of the [Mg/Fe] abundance ratio in the solar neighbourhood and show how this is consistent with recent observations combining the APOGEE DR16 data (chemical abundances) and the astroNN catalogue (stellar ages, orbital parameters). We computed the vertical maximum heights $|z_{\rm max}|$, using the Ting & Rix (2019) relation to compute the orbits around the Galaxy of SSPs born at different evolutionary times. Our main conclusions can be summarised as follows:

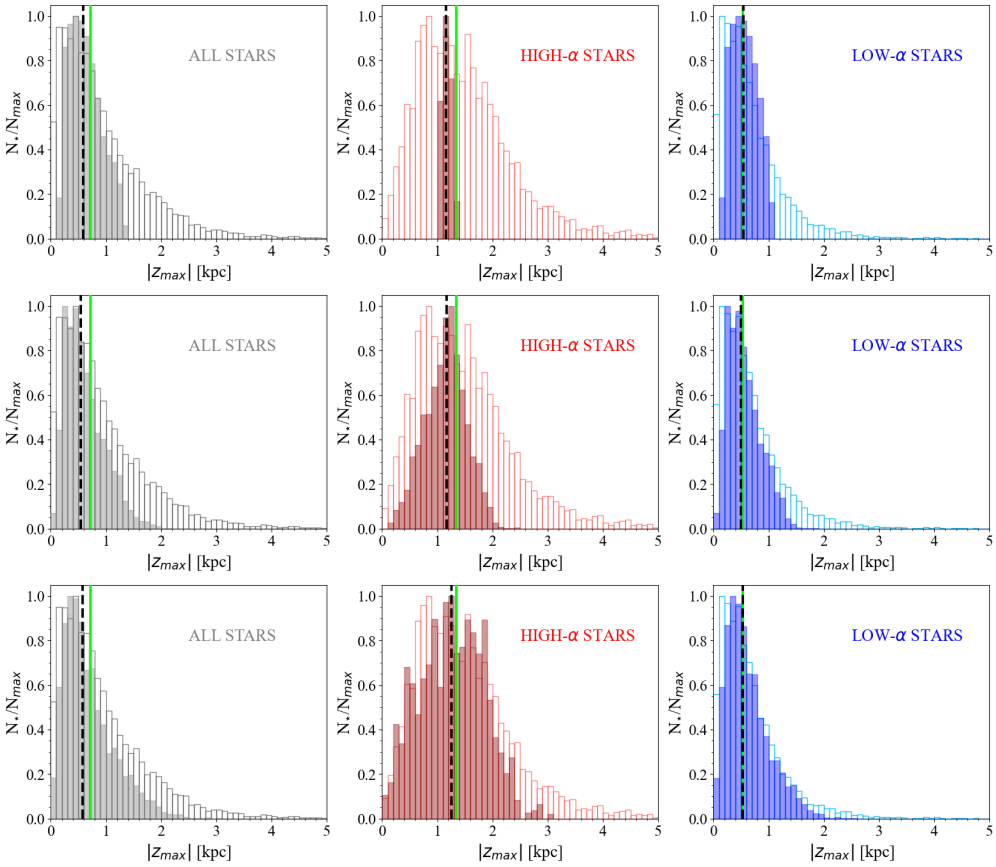

Fig. 13. As in Fig. 7 but for the ES20 model.

1. Regarding the vertical [Mg/Fe] abundance distributions, we find better agreement between models by Spitoni et al. (2020, 2021) and the combined APOGEE DR16 data and astroNN catalogue (for stellar ages younger than 8 Gyr) for stars close to the Galactic midplane $|z| < 2$ kpc.
2. The distribution of the initial vertical velocities $v_{0,z}(\tau)$ as a function of the Galactic age τ for the computed SSPs can be interpreted as the upper limit on the observed vertical velocity dispersion σ_z versus age relation in the solar vicinity.
3. Extending the Ting & Rix (2019) relation to the whole stellar age range, the predicted curves for the vertical [Mg/Fe] distribution by the models nicely overlap with the regions characterised by the highest densities of stars in both low-α and high-α APOGEE sequences with observed heights $|z| < 2$ kpc. However, the median values of APOGEE data in the high-α sequence generally show a steeper growth of $|z_{\rm max}|$ compared to model predictions. This is due to the fact that, in the past, the Milky Way may have been affected by important merger episodes, and such external perturbations could have heated up the thick disc. Hence, an extra-vertical action J_z component is missing if we consider stellar scattering as the only heating process, as assumed by Ting & Rix (2019).
4. Assuming a disc dissection based on chemistry for APOGEE-DR16 stars ($|z| < 2$ kpc), the observed $|z_{\rm max}|$ distributions for high-α and low-α sequences are in good agreement with our model predictions if, in the calculation, we consider an error in the vertical action $\widehat{J_z}$ of Ting & Rix (2019) with standard deviation $\sigma_{J_z} = 1 \cdot J_z$ (such an error

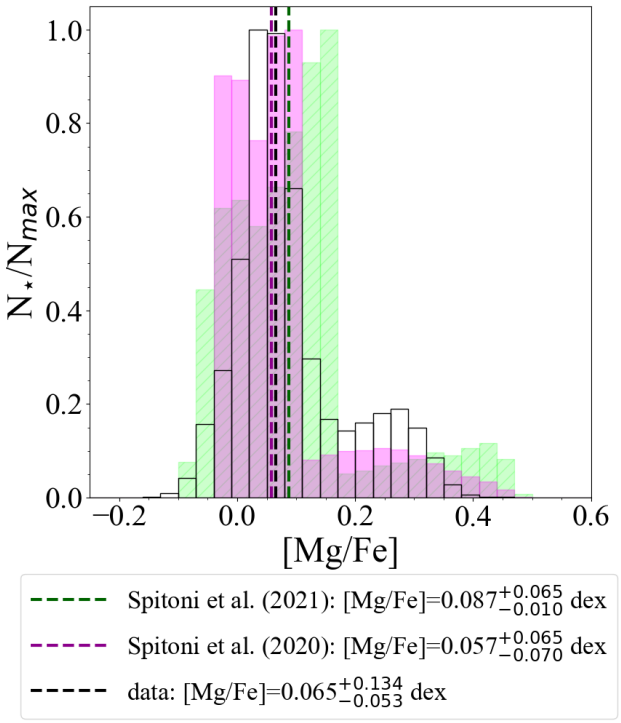

Fig. 14. [Mg/Fe] distributions predicted by the ES21 model computed at 8 kpc (green histogram) and by the *M2* model of ES20 (magenta histogram) compared with the APOGEE DR16 data (black empty histogram) for stars with Galactocentric distances of between 6 and 10 kpc. Black, green, and magenta vertical dashed lines indicate the median values of the data and models.

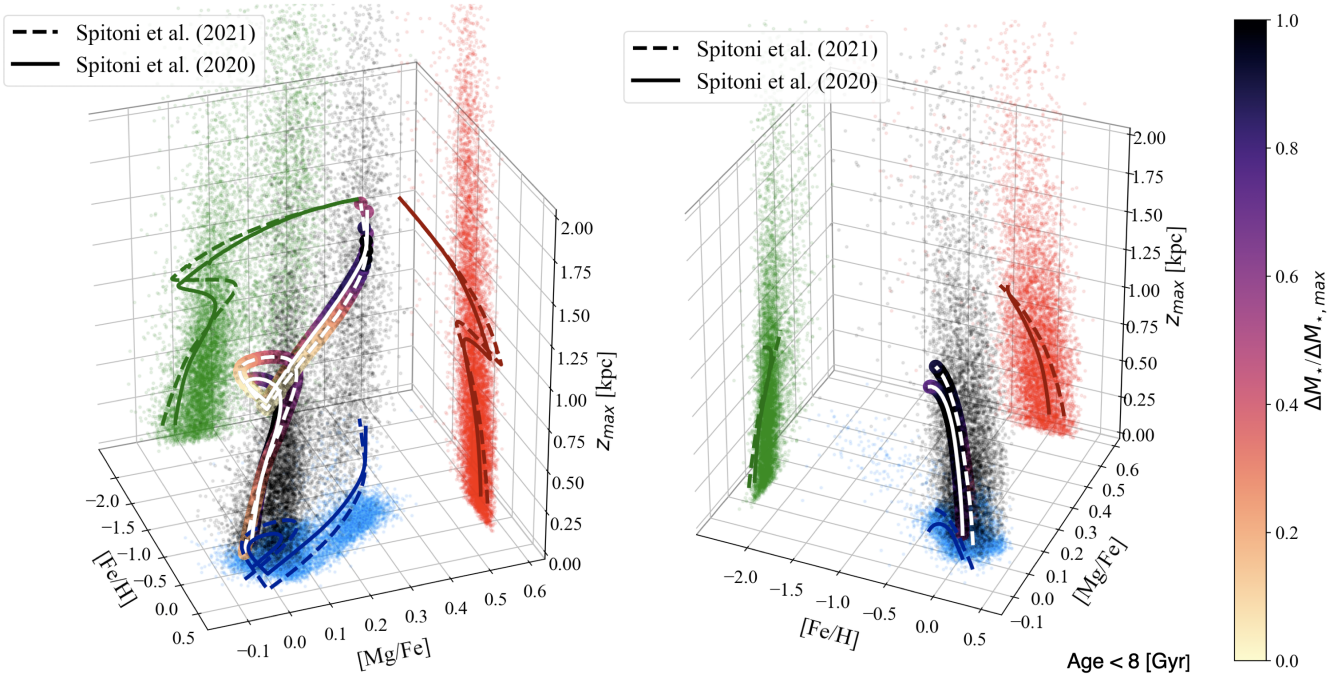

Fig. 15. Observed stars (grey points) in the 3D space formed by APOGEE DR16 abundance ratios (i.e. [Fe/H] and [Mg/Fe]) and maximum vertical excursion from the midplane $|z_{max}|$ (from astroNN catalogue) in the Galactic region between 6 and 10 kpc with $|z| < 2$ kpc compared with model predictions by ES20 and ES21 (white solid and dashed lines, respectively). The associated projections are drawn with red, blue, and green points (data) and lines (models), respectively. In the *left panel* all the stellar ages have been considered, while in the right one only observed and predicted stars younger than 8 Gyr have been drawn. In *both panels*, the colour-coded points indicate the predicted surface stellar mass density $\Delta M_\star$ formed in constant age intervals fixed at the value of 0.05 Gyr normalised to the maximum value $\Delta M_{\star,\max}$.

is inspired by the study of Gandhi & Ness 2019 based on GALAH stars and Ting & Rix 2019).

5. When we also include information about the predicted surface stellar mass density throughout the chemical evolution in Spitoni et al. (2021) model results, there is tension between the location of most densely populated regions in APOGEE DR16 stars and the model peaks in the $|z_{max}|$ versus [Mg/Fe] relation if we consider the full stellar age range. Moreover, the Spitoni et al. (2021) model forms too many stars as soon as the first infall begins, and in the $|z_{max}|$ versus [Mg/Fe] many stars are predicted in a region where APOGEE DR16 stars are rare. This is due to the best-fit model parameter value for the infall timescale τ_1 of the high-α sequence being quite short (i.e. ∼0.1 Gyr).
6. On the contrary, model *M2* by Spitoni et al. (2020) characterised by longer timescales of accretion (see Table 1) reproduces the above-mentioned bimodality in the $|z_{max}|$ versus [Mg/Fe] relation. The distribution of the formed stars predicted by the Spitoni et al. (2020) model in the $|z_{max}|$ versus [Mg/Fe] relation shows no tension with the data. Indeed, the two peaks of the predicted stellar mass density are in correspondence to the highest density regions in the data. We conclude inclusion of precise stellar ages inferred from asteroseismology is necessary to properly constrain chemical evolution models of the Milky Way disc components.
7. The distributions of the predicted SSPs in the $|z_{max}|$ versus [Mg/Fe] space, including the observed dispersion in the vertical action J_z estimates, show the presence of the disc dichotomy signature, in good agreement with data.

We have shown that in the vertical distribution of the [Mg/Fe] abundance ratios a dichotomy merges from the analysis of the APOGEE data. In conclusion, we found that the signature of a delayed gas infall episode, which gives rise to a hiatus in the star formation history of the Galaxy, are imprinted both in the [Mg/Fe] versus [Fe/H] relation and in vertical distribution of [Mg/Fe] abundances in the solar vicinity.

Acknowledgements. The authors thank the referee F. Vincenzo for various suggestions that improved the paper. E. Spitoni thanks A. Recio-Blanco and P.A. Palicio for useful discussions. E. Spitoni received funding from the European Union's Horizon 2020 research and innovation program under SPACE-H2020 grant agreement number 101004214 (EXPLORE project). E. Spitoni acknowledges support from the ERC Consolidator Grant (Hungary) programme (Project RADIOSTAR, G.A. n. 724560). Funding for the Stellar Astrophysics Centre is provided by The Danish National Research Foundation (Grant agreement no.: DNRF106). E. Spitoni and V. Aguirre Børsen-Koch acknowledge support from the Independent Research Fund Denmark (Research grant 7027-00096B). This work was partially supported by the program Unidad de Excelencia María de Maeztu CEX2020-001058-M. K. Verma is supported by the Juan de la Cierva fellowship (IJC2019-041344-I). A. Stokholm acknowledges support from the European Research Council Consolidator Grant funding scheme (project ASTEROCHRONOMETRY, G.A. n. 772293, http://www.asterochronometry.eu). In this work, we have made use of SDSS-IV APOGEE-2 DR16 data. Funding for the Sloan Digital Sky Survey IV has been provided by the Alfred P. Sloan Foundation, the U.S. Department of Energy Office of Science, and the Participating Institutions. SDSS-IV acknowledges support and resources from the Center for High-Performance Computing at the University of Utah. The SDSS web site is www.sdss.org. SDSS is managed by the Astrophysical Research Consortium for the Participating Institutions of the SDSS Collaboration which are listed at www.sdss.org/collaboration/affiliations/. With this paper we also made use of the Python package for Galactic dynamics GALPY (http://github.com/jobovy/galpy).

References

Ablimit, I., Zhao, G., Flynn, C., & Bird, S. A. 2020, ApJ, 895, L12
Agertz, O., Renaud, F., Feltzing, S., et al. 2021, MNRAS, 503, 5826
Aguirre Børsen-Koch, V., Rørsted, J. L., Justesen, A. B., et al. 2022, MNRAS, 509, 4344
Ahumada, R., Allende Prieto, C., Almeida, A., et al. 2020, ApJS, 249, 3
Beane, A., Ness, M. K., & Bedell, M. 2018, ApJ, 867, 31

Binney, J. 2010, MNRAS, 401, 2318
Binney, J., & Spergel, D. 1984, MNRAS, 206, 159
Bird, J. C., Kazantzidis, S., Weinberg, D. H., et al. 2013, ApJ, 773, 43
Bovy, J. 2015, ApJS, 216, 29
Brook, C. B., Stinson, G. S., Gibson, B. K., et al. 2012, MNRAS, 426, 690
Buck, T. 2020, MNRAS, 491, 5435
Buder, S., Lind, K., Ness, M. K., et al. 2019, A&A, 624, A19
Buder, S., Sharma, S., Kos, J., et al. 2021, MNRAS, 506, 150
Carlberg, R. G. 1987, ApJ, 322, 59
Cescutti, G., Matteucci, F., François, P., & Chiappini, C. 2007, A&A, 462, 943
Chiappini, C., Matteucci, F., & Gratton, R. 1997, ApJ, 477, 765
Chiappini, C., Matteucci, F., & Meynet, G. 2003, A&A, 410, 257
Chieffi, A., & Limongi, M. 2013, ApJ, 764, 21
Clarke, A. J., Debattista, V. P., Nidever, D. L., et al. 2019, MNRAS, 484, 3476
Conroy, C., Naidu, R. P., Garavito-Camargo, N., et al. 2021, Nature, 592, 534
Côté, B., O'Shea, B. W., Ritter, C., Herwig, F., & Venn, K. A. 2017, ApJ, 835, 128
D'Onghia, E., Madau, P., Vera-Ciro, C., Quillen, A., & Hernquist, L. 2016, ApJ, 823, 4
Duong, L., Freeman, K. C., Asplund, M., et al. 2018, MNRAS, 476, 5216
Foreman-Mackey, D., Hogg, D. W., Lang, D., & Goodman, J. 2013, PASP, 125, 306
François, P., Matteucci, F., Cayrel, R., et al. 2004, A&A, 421, 613
Fuhrmann, K., Chini, R., Kaderhandt, L., & Chen, Z. 2017, MNRAS, 464, 2610
Gaia Collaboration (Katz, D., et al.) 2018, A&A, 616, A11
Gandhi, S. S., & Ness, M. K. 2019, ApJ, 880, 134
Gómez, F. A., Minchev, I., O'Shea, B. W., et al. 2013, MNRAS, 429, 159
Goodman, J., & Weare, J. 2010, Commun. Appl. Math. Comput. Sci., 5, 65
Grand, R. J. J., Bustamante, S., Gómez, F. A., et al. 2018, MNRAS, 474, 3629
Greggio, L., & Renzini, A. 1983, A&A, 118, 217
Hayden, M. R., Bovy, J., Holtzman, J. A., et al. 2015, ApJ, 808, 132
Helmi, A., Babusiaux, C., Koppelman, H. H., et al. 2018, Nature, 563, 85
House, E. L., Brook, C. B., Gibson, B. K., et al. 2011, MNRAS, 415, 2652
Iwamoto, K., Brachwitz, F., Nomoto, K., et al. 1999, ApJS, 125, 439
Johnson, J. W., Weinberg, D. H., Vincenzo, F., et al. 2021, MNRAS, 508, 4484
Kazantzidis, S., Zentner, A. R., Kravtsov, A. V., Bullock, J. S., & Debattista, V. P. 2009, ApJ, 700, 1896
Kennicutt, R. C., Jr 1998, ApJ, 498, 541
Khoperskov, S., Haywood, M., Snaith, O., et al. 2021, MNRAS, 501, 5176
Kobayashi, C., & Nakasato, N. 2011, ApJ, 729, 16
Kobayashi, C., Karakas, A. I., & Lugaro, M. 2020, ApJ, 900, 179
Kroupa, P. 2002, in Modes of Star Formation and the Origin of Field Populations, eds. E. K. Grebel, & W. Brandner, ASP Conf. Ser., 285, 86
Kroupa, P. 2008, in Pathways Through an Eclectic Universe, eds. J. H. Knapen, T. J. Mahoney, & A. Vazdekis, ASP Conf. Ser., 390, 3
Leung, H. W., & Bovy, J. 2019, MNRAS, 489, 2079
Lian, J., Thomas, D., Maraston, C., et al. 2020, MNRAS, 494, 2561
Loebman, S. R., Roškar, R., Debattista, V. P., et al. 2011, ApJ, 737, 8
Mackereth, J. T., & Bovy, J. 2018, PASP, 130, 114501
Mackereth, J. T., Bovy, J., Leung, H. W., et al. 2019, MNRAS, 489, 176
Matteucci, F. 2012, Chemical Evolution of Galaxies (Berlin Heidelberg: Springer-Verlag)
Matteucci, F. 2021, A&ARv, 29, 5
Matteucci, F., & Greggio, L. 1986, A&A, 154, 279
McKee, C. F., Parravano, A., & Hollenbach, D. J. 2015, ApJ, 814, 13
Melioli, C., Brighenti, F., D'Ercole, A., & de Gouveia Dal Pino, E. M. 2008, MNRAS, 388, 573
Melioli, C., Brighenti, F., D'Ercole, A., & de Gouveia Dal Pino, E. M. 2009, MNRAS, 399, 1089
Mikolaitis, Š., Hill, V., Recio-Blanco, A., et al. 2014, A&A, 572, A33
Mikolaitis, S., de Laverny, P., Recio-Blanco, A., et al. 2017, A&A, 600, A22
Minchev, I., & Famaey, B. 2010, ApJ, 722, 112
Minchev, I., Famaey, B., Quillen, A. C., et al. 2012, A&A, 548, A126
Miyamoto, M., & Nagai, R. 1975, PASJ, 27, 533
Moetazedian, R., & Just, A. 2016, MNRAS, 459, 2905
Mott, A., Spitoni, E., & Matteucci, F. 2013, MNRAS, 435, 2918
Navarro, J. F., Frenk, C. S., & White, S. D. M. 1996, ApJ, 462, 563
Ness, M. K., Johnston, K. V., Blancato, K., et al. 2019, ApJ, 883, 177
Nidever, D. L., Bovy, J., Bird, J. C., et al. 2014, ApJ, 796, 38
Nissen, P. E., Christensen-Dalsgaard, J., Mosumgaard, J. R., et al. 2020, A&A, 640, A81
Nitschai, M. S., Eilers, A.-C., Neumayer, N., Cappellari, M., & Rix, H.-W. 2021, ApJ, 916, 112
Noguchi, M. 2018, Nature, 559, 585
Palla, M., Matteucci, F., Spitoni, E., Vincenzo, F., & Grisoni, V. 2020, MNRAS, 498, 1710
Prantzos, N., Abia, C., Limongi, M., Chieffi, A., & Cristallo, S. 2018, MNRAS, 476, 3432
Queiroz, A. B. A., Anders, F., Chiappini, C., et al. 2020, A&A, 638, A76
Quinn, P. J., Hernquist, L., & Fullagar, D. P. 1993, ApJ, 403, 74
Recio-Blanco, A., de Laverny, P., Kordopatis, G., et al. 2014, A&A, 567, A5
Ritter, C., Herwig, F., Jones, S., et al. 2018, MNRAS, 480, 538
Rojas-Arriagada, A., Recio-Blanco, A., de Laverny, P., et al. 2016, A&A, 586, A39
Rojas-Arriagada, A., Recio-Blanco, A., de Laverny, P., et al. 2017, A&A, 601, A140
Romano, D., Karakas, A. I., Tosi, M., & Matteucci, F. 2010, A&A, 522, A32
Santos-Peral, P., Recio-Blanco, A., Kordopatis, G., Fernández-Alvar, E., & de Laverny, P. 2021, A&A, 653, A85
Scalo, J. M. 1986, Fund Cosmic. Phys., 11, 1
Schlesinger, K. J., Johnson, J. A., Rockosi, C. M., et al. 2014, ApJ, 791, 112
Schönrich, R., & Binney, J. 2009, MNRAS, 396, 203
Sellwood, J. A. 2013, ApJ, 769, L24
Sellwood, J. A., & Binney, J. J. 2002, MNRAS, 336, 785
Sharma, S., Hayden, M. R., Bland-Hawthorn, J., et al. 2021, MNRAS, 506, 1761
Silva Aguirre, V., Davies, G. R., Basu, S., et al. 2015, MNRAS, 452, 2127
Silva Aguirre, V., Lund, M. N., Antia, H. M., et al. 2017, ApJ, 835, 173
Silva Aguirre, V., Bojsen-Hansen, M., Slumstrup, D., et al. 2018, MNRAS, 475, 5487
Snaith, O. N., Bailin, J., Gibson, B. K., et al. 2016, MNRAS, 456, 3119
Solway, M., Sellwood, J. A., & Schönrich, R. 2012, MNRAS, 422, 1363
Spitoni, E., & Matteucci, F. 2011, A&A, 531, A72
Spitoni, E., Recchi, S., & Matteucci, F. 2008, A&A, 484, 743
Spitoni, E., Matteucci, F., Recchi, S., Cescutti, G., & Pipino, A. 2009, A&A, 504, 87
Spitoni, E., Matteucci, F., & Sozzetti, A. 2014, MNRAS, 440, 2588
Spitoni, E., Romano, D., Matteucci, F., & Ciotti, L. 2015, ApJ, 802, 129
Spitoni, E., Gioannini, L., & Matteucci, F. 2017, A&A, 605, A38
Spitoni, E., Silva Aguirre, V., Matteucci, F., Calura, F., & Grisoni, V. 2019a, A&A, 623, A60
Spitoni, E., Cescutti, G., Minchev, I., et al. 2019b, A&A, 628, A38
Spitoni, E., Verma, K., Silva Aguirre, V., & Calura, F. 2020, A&A, 635, A58
Spitoni, E., Verma, K., Silva Aguirre, V., et al. 2021, A&A, 647, A73
Ting, Y.-S., & Rix, H.-W. 2019, ApJ, 878, 21
Ting, Y.-S., Hawkins, K., & Rix, H.-W. 2018, ApJ, 858, L7
van den Hoek, L. B., & Groenewegen, M. A. T. 1997, A&AS, 123, 305
Velazquez, H., & White, S. D. M. 1999, MNRAS, 304, 254
Vera-Ciro, C., & D'Onghia, E. 2016, ApJ, 824, 39
Verma, K., Grand, R. J. J., Silva Aguirre, V., & Stokholm, A. 2021, MNRAS, 506, 759
Vincenzo, F., & Kobayashi, C. 2020, MNRAS, 496, 80
Vincenzo, F., Spitoni, E., Calura, F., et al. 2019, MNRAS, L74
Vincenzo, F., Weinberg, D. H., Miglio, A., Lane, R. R., & Roman-Lopes, A. 2021, MNRAS, 508, 5903
Walker, I. R., Mihos, J. C., & Hernquist, L. 1996, ApJ, 460, 121
Weinberg, D. H., Holtzman, J. A., Hasselquist, S., et al. 2019, ApJ, 874, 102
Woosley, S. E., & Weaver, T. A. 1995, ApJS, 101, 181
Yu, Z., Li, J., Chen, B., et al. 2021, ApJ, 912, 106